J. Fluid Mech. (2013), *vol.* 733, *pp.* 68–99.
doi:10.1017/jfm.2013.437

Temporal stability of eccentric Taylor–Couette–Poiseuille flow

Colin Leclercq†, Benoît Pier and Julian F. Scott

Laboratoire de mécanique des fluides et d'acoustique, École centrale de Lyon – CNRS – Université Claude-Bernard Lyon 1 – INSA Lyon, 36 avenue Guy-de-Collongue, 69134 Écully CEDEX, France

(Received 23 February 2013; revised 27 June 2013; accepted 16 August 2013)

The combined effects of axial flow and eccentricity on the temporal stability properties of the Taylor–Couette system are investigated using a pseudospectral method. Eccentricity is found to stabilize the Couette flow regardless of axial advection intensity. As the axial Reynolds number Re_z is increased for any fixed eccentricity $e \leqslant 0.7$, the critical mode switches from deformed toroidal Taylor vortices to helical structures with an increasing number of waves, and with helicity opposed to the inner-cylinder rotation. For a wide-gap configuration of radius ratio $\eta = 0.5$, increasing axial advection has a stabilizing effect for low Re_z, then a weak destabilizing effect for high enough Re_z. Centrifugal effects are always destabilizing, but axial shear is responsible for the dominance of helical modes of increasing azimuthal complexity. The modes localize in the converging gap region, and the energy concentrates increasingly into axial motion for larger Re_z. Critical quantities are also computed for a small-gap case, and similar trends are observed, even though no destabilizing effect of advection is observed within the range of Re_z considered. Comparison with the experiment of Coney & Mobbs (*Proc. Inst. Mech. Engrs*, vol. 184 Pt 3L, 1969–70, pp. 10–17) for $\eta = 0.89$ shows good agreement, despite small discrepancies attributed to finite length effects.

Key words: convection, instability, Taylor–Couette flow

1. Introduction

More than 40 years ago, Coney & Mobbs (1969–70) wrote: 'a linear stability theory solution for the case of eccentric rotating cylinders with a superimposed axial flow [...] is not available and the difficulties in the way of such a solution are formidable'. Indeed, while the flow between rotating cylinders has been one of the benchmarks of hydrodynamic stability since the path-breaking work of Taylor (1923), the computational cost associated with more complex versions of this flow has long been considered a showstopper, and still remains a major challenge as we try to bridge the gap with engineering applications. In this paper, we study the temporal stability of cylindrical Couette flow with two additional effects: eccentricity of the cylinder axes and axial flow. Taken separately, the two effects have already been the subject of numerous studies, which we will briefly review in this introductory section. But to the

† Email address for correspondence: colin.leclercq@ec-lyon.fr

best of our knowledge, no one has yet undertaken the complete theoretical study of the combination of both, and very limited experimental data are available in this case.

1.1. *Control parameters*

This problem is governed by four control parameters. The geometry is defined by the ratio of radii $0 < \eta \equiv a/b < 1$ and eccentricity $0 \leqslant e \equiv c/(b-a) \leqslant 1$, where a and b are the inner and outer cylinder radii and c is the distance between centres. Introducing the clearance $d = b - a$, one can also use the clearance ratio $\delta \equiv d/a = (1-\eta)/\eta$ instead of η.

The azimuthal Reynolds number $Re_\Omega = a\Omega d/\nu$, based on the inner-cylinder rotation rate Ω, compares centrifugal and viscous effects, while the axial Reynolds number $Re_z = \overline{w}d/\nu$, based on the mean axial velocity $\overline{w}$, measures the importance of axial advection.

1.2. *Industrial applications: wellbore drilling and high-speed journal bearings*

This model flow is of interest to the oil industry as a first step towards understanding the dynamics of the complex annular flow of mud in wellbore drilling operations. For drilling applications, a drillstring is rotated inside the well in order to drive a drill bit that cuts the rock at the bottom of the well. Mud is injected through the drillstring and flows back to the surface through the annular gap, ensuring several engineering functions, among which are the following (Escudier, Oliveira & Pinho 2002): carrying the rock cuttings out of the well, cooling and cleaning the drill bit, supporting the wellbore, avoiding inflow of formation fluids and preventing settling of the cuttings when circulation is stopped. The annular flow of mud can be modelled in a first approximation by an eccentric Taylor–Couette–Poiseuille flow because of the rotation of the drillstring, the pressure-driven axial flow and eccentricity caused by flexibility of the drillstring.

For typical industrial configurations (Escudier *et al.* 2002; Guo & Liu 2011), the ratio between drillstring and outer-wall radii ranges from 0.2 at the top to 0.8 at the bottom, and the eccentricity can go all the way to the limit of touching cylinders. The gap between the drillstring and the outer wall is of order 10^{-2}–10^{-1} m. The velocity of the inner cylinder in rotation is comparable to the mean axial velocity of the flow, of the order of 1 m s^{-1}. Finally, the mud density is of order 10^3 kg m^{-3}, with an equivalent dynamic viscosity in the range 10^{-3}–10^{-1} Pa s (note that viscosity is a function of local strain rate for non-Newtonian fluids). As a result, equivalent Reynolds numbers Re_Ω and Re_z of the order of 10^2–10^5 are expected.

Limitations of the model for this application include non-Newtonian effects (viscoelasticity and thixotropicity), motion of the inner-cylinder position inside the well, contamination of the fluid by cuttings and 'formation fluid', variable eccentricity and outer-wall radius with depth, and imperfect circularity of the wellbore wall. However, the consideration of both eccentricity and axial flow in a systematic way is already a significant improvement on existing theory.

Eccentric Taylor–Couette–Poiseuille flow is also of interest in the field of high-speed journal bearings, where 'the damaging effect of impurities contained in oil can be considerably reduced when they are quickly removed from the friction contact area [...] by intensifying axial oil flow' (Sep 2008). In high-speed journal bearings, Huggins (1966–67) quotes a value of $Re_z = 100$ during tests on a 24 in diameter journal bearing. And instabilities are expected to arise, as noted by Coney & Mobbs (1969–70): 'in the large-diameter journal bearings, which may be expected to operate

in the Taylor vortex régime, there is [...] a considerable superimposed axial flow of lubricant'.

1.3. *Eccentric Taylor–Couette flow*

The effect of eccentricity on the Taylor–Couette flow has been investigated by many researchers, covering a wide range of ratio of radii and eccentricities, starting with the experimental work of Cole (1957). Using torque measurements, flow visualization (dye injection, aluminum flakes etc.) and hot-wire probes, Cole (1957, 1967, 1969), Kamal (1966), Vohr (1968), Koschmieder (1976) and later Karasudani (1987), Xiao, Lim & Chew (1997) and Lim & Lim (2008) found a stabilizing effect of eccentricity on the appearance of Taylor vortices. On the other hand, Castle & Mobbs (1967), Versteegen & Jankowski (1969) and Frêne & Godet (1971) found a slight destabilization at weak eccentricities, followed by stabilization at higher values. The vortices of the first type, confined to the neighbourhood of the inner cylinder, were later found to be caused by endwall effects by Mobbs & Ozogan (1984) and El-Dujaily & Mobbs (1990). For the second type of vortices, an increase in critical wavenumber at higher eccentricities was reported in the early work of Cole (1967) and quantified by subsequent authors.

The first theoretical analyses were made by DiPrima (1963) and Ritchie (1968), using local stability theory (as implied by the parallel-flow approximation in the 'pseudo-azimuthal' direction) and asymptotic analyses in the small-gap, small-eccentricity limit. The first global stability analyses of the problem, considering fully two-dimensional basic flows, were performed a decade later by DiPrima & Stuart (1972*b*), DiPrima & Stuart (1975) and Eagles, Stuart & DiPrima (1978), demonstrating a stabilizing effect of eccentricity and the weakness of the local approach to model this flow. More recently, Oikawa, Karasudani & Funakoshi (1989*a*,*b*) and Dai, Dong & Szeri (1992) were able to relax the small-gap and small-eccentricity constraint (e up to 0.6–0.7, η as low as 0.5), using numerical methods to solve the two-dimensional stability problem.

Finally, most recent numerical and experimental stability analyses seem to have been concerned mostly with the effect of non-Newtonian fluids (e.g. Chawda & Avgousti 1996; Dris & Shaqfeh 1998), with applications to oil drilling and polymeric processing.

1.4. *Taylor–Couette–Poiseuille flow*

The effect of a pressure-driven axial flow on the concentric Taylor–Couette system with a fixed outer cylinder has been the object of even more investigations. The first analytical studies were restricted to the narrow-gap limit and axisymmetric perturbations (e.g. Chandrasekhar 1960; DiPrima 1960), reaching (after some controversy) the conclusion that advection stabilizes the Couette flow. The first correct numerical studies of the finite-gap geometry, with non-axisymmetric disturbances, are due to Takeuchi & Jankowski (1981) and Ng & Turner (1982). For a wide-gap configuration $\eta = 0.5$, Takeuchi & Jankowski (1981) confirmed numerically and experimentally (for respectively $Re_z \leqslant 100$ and $Re_z \leqslant 150$) the results from Snyder (1962, 1965)'s experiments showing that toroidal vortices are replaced by helical vortices for larger advection rates. Ng & Turner (1982) extended the results to $Re_z \leqslant 6000$ for $\eta = 0.77$ and $\eta = 0.95$, with fair agreement with experiments. They also considered axisymmetric disturbances for $\eta = 0.95$ up to the value of $Re_z = 7739.5$, where annular Poiseuille flow becomes unstable with respect to Tollmien–Schlichting (TS) like disturbances. They showed a connection between the

centrifugal instability and the shear instability at high advection rates, as conjectured by Reid (1961). More recently, Cotrell & Pearlstein (2004) and Cotrell, Sarma & Pearlstein (2004) extended the analysis of Ng & Turner (1982) to non-axisymmetric disturbances for $\eta = 0.5, 0.77, 0.95$. Before the transition to shear instability, these authors noted the existence of a plateau in critical Re_Ω, for which the associated critical axial wavenumber drops with increasing Re_z. For the case $\eta = 0.5$, they also noticed the existence of a maximum critical Re_Ω for a specific value of Re_z. Heaton (2008) complemented their analyses by assessing the importance of non-modal effects, and showed their relevance at moderate and large $Re_z \sim 10^2$–10^4. Other recent studies concern rotation of the outer cylinder (Meseguer & Marques 2002), absolute/convective instabilities (Altmeyer, Hoffmann & Lücke 2011), supercritical states (Hwang & Yang 2004), time-periodic flow (Marques & Lopez 2000), additional radial flow (e.g. Martinand, Serre & Lueptow 2009) and so on. A comprehensive review of the large panel of work on this topic, though not completely up to date, is available in Cotrell & Pearlstein (2004).

1.5. *Eccentric Taylor–Couette–Poiseuille flow*

As already mentioned, some experimental data are available in the case of combined eccentricity and axial flow. To the best of the authors' knowledge, only one experiment has been undertaken, at a radius ratio of $\eta = 0.89$ (Coney & Mobbs 1969–70; Coney 1971; Younes 1972; Younes, Mobbs & Coney 1972; Mobbs & Younes 1974; Coney & Atkinson 1978). In Coney & Mobbs (1969–70) and Younes *et al.* (1972), the critical Taylor number is reported as a function of $e \leqslant 0.8$ and Re_z up to 125, using flow visualization and torque measurements. It is found that axial flow always stabilizes the Couette flow. At fixed eccentricity, stabilization due to advection is less marked than in the concentric case. The critical curves have complicated forms for $Re_z \geqslant 75$, but the effect of eccentricity is generally stabilizing. However, the results display considerable scatter and are very sensitive to the instability criterion, as shown in Coney & Atkinson (1978). Moreover, attempts at determining the critical wavenumber of the perturbations proved abortive, because of the complex flow structure observed. For $e > 0.2$, $Re_z > 20$, there seems to be coexistence of two helical structures winding in opposite directions, with 'fluctuations in the number of vortex cells occupying the length of the apparatus at any instant or in the number of turns in the vortex spirals' (Coney & Mobbs 1969–70; Mobbs & Younes 1974). These experiments will be discussed further in § 4.

On the theoretical side, apart from the semi-empirical local stability theory of Coney & Mobbs (1969–70), inspired by the work of DiPrima (1963), no stability analysis has been attempted so far. Modal stability analysis is the object of the present paper and is a first step towards understanding the complex behaviour exhibited by this flow.

1.6. *Plan of the paper*

The paper is organized into four sections. Section 2 introduces the linear stability problem, including governing equations and numerical methods for basic-flow and normal-mode computations. The main properties of the basic flow and dominant eigenmodes are presented. In § 3, a parametric temporal stability study is performed for $\eta = 0.5$: critical quantities are computed and stability diagrams are given. The instability mechanism is investigated by examining the spatial structure of the critical modes, and variations of growth rates with control parameters. In § 4, critical values are computed for a small-gap case $\eta = 0.89$, for which comparison with experimental

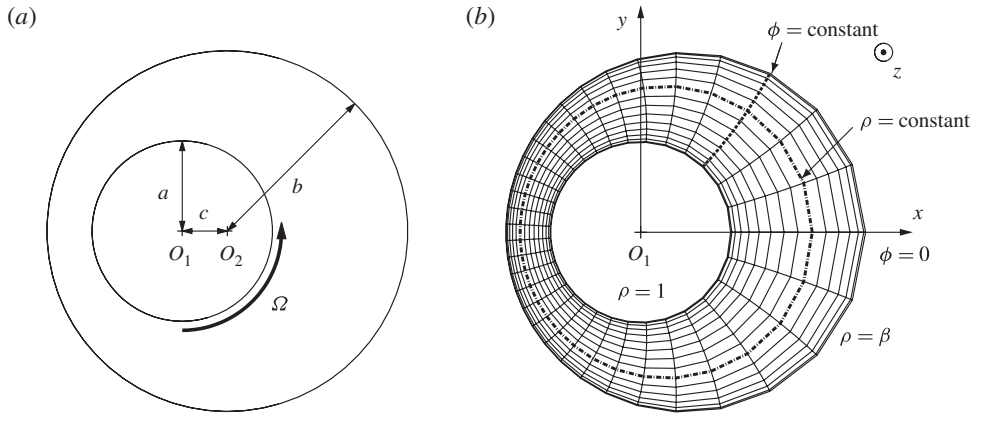

FIGURE 1. The eccentric annular domain for radius ratio $\eta = 0.5$ and eccentricity $e = 0.5$. (*a*) Definition of the geometry. (*b*) A typical bipolar mesh used for calculations with $N_\xi = K_\phi = 16$.

data is possible. A concluding section then summarizes our main findings and paves the way for future work.

2. Linear stability framework

Recall that a, b are the inner and outer cylinder radii, $d = b - a$ is the clearance and Ω is the rotation rate of the inner cylinder, while ρ and ν are the density and the kinematic viscosity. In the following, quantities will be made non-dimensional with respect to the reference scales $L \equiv d$, $V \equiv a\Omega$ and $P \equiv \rho V^2$ for length, velocity and pressure.

An azimuthal/rotational Reynolds number, defined as $Re_\Omega \equiv VL/\nu = a\Omega d/\nu$, will be used to measure competition between centrifugal effects and viscosity. Note that this type of definition is preferred in recent numerical work (e.g. Oikawa *et al.* 1989*a*; Feng, Li & Fu 2007; Martinand *et al.* 2009) rather than using Taylor numbers of the form $\mathrm{Ta} \sim \delta Re_\Omega^2$, which naturally appeared in the pioneering analytical studies of the small-gap limit $\delta \to 0$ (e.g. Taylor 1923; DiPrima 1959; Chandrasekhar 1981).

Axial advection is characterized by an axial Reynolds number $Re_z \equiv \overline{w}d/\nu$, based on the mean axial velocity $\overline{w}$. The ratio Re_z/Re_Ω represents the mean axial velocity in units of rotation velocity, and conveniently measures competition between advection and rotation. Because of this, the use of an azimuthal Reynolds number instead of a 'classical' Taylor number seems particularly appropriate when axial flow is considered.

Finally, the geometry is characterized by the ratio of radii $0 < \eta \equiv a/b < 1$ or, equivalently, the clearance ratio $\delta \equiv d/a = (1 - \eta)/\eta$. The eccentricity is measured by the non-dimensional number $0 \leqslant e = c/d \leqslant 1$, where c is the distance between centres (cf. figure 1).

2.1. *Governing equations*

The incompressible Navier–Stokes equations governing velocity $\boldsymbol{u}$ and pressure p read

$$\left.\begin{aligned} \partial_t \boldsymbol{u} + \boldsymbol{u}\cdot\boldsymbol{\nabla}\boldsymbol{u} &= -\boldsymbol{\nabla}p + Re_\Omega^{-1}\nabla^2\boldsymbol{u}, \\ \boldsymbol{\nabla}\cdot\boldsymbol{u} &= 0, \end{aligned}\right\} \tag{2.1}$$

with impermeability and no-slip boundary conditions at the walls (rotating inner cylinder, fixed outer one). Basic flows for stability analyses are axially invariant, steady solutions of (2.1). Because of the vanishing derivatives in the axial direction $\boldsymbol{e}_z$, velocity components $\boldsymbol{u}_\perp = \boldsymbol{u} - w\boldsymbol{e}_z$ perpendicular to the axis are decoupled from the axial component w. Letting the subscript '$\perp$' denote projection perpendicular to $\boldsymbol{e}_z$, $\boldsymbol{u}_\perp$ satisfies

$$\left.\begin{aligned} \partial_t \boldsymbol{u}_\perp + \boldsymbol{u}_\perp \cdot \boldsymbol{\nabla}_\perp \boldsymbol{u}_\perp &= -\boldsymbol{\nabla}_\perp p + Re_\Omega^{-1} \nabla_\perp^2 \boldsymbol{u}_\perp, \\ \boldsymbol{\nabla}_\perp \cdot \boldsymbol{u}_\perp &= 0. \end{aligned}\right\} \tag{2.2}$$

Steady solutions of (2.2), with boundary conditions, yield 'in-plane' components $\boldsymbol{u}_{B,\perp}$ of basic flows, denoted in what follows as $\boldsymbol{u}_B = (\boldsymbol{u}_{B,\perp}, w_B)$. The basic axial velocity can then be calculated by simply solving a linear system

$$\boldsymbol{u}_{B,\perp} \cdot \boldsymbol{\nabla}_\perp w_B = -G + Re_\Omega^{-1} \nabla_\perp^2 w_B, \tag{2.3}$$

where G is the imposed axial pressure gradient. Wood (1957)'s modified bipolar coordinate system (ρ, ϕ), fitting the annular domain (see figure 1) with the following conformal transformation, is appropriate for the present configuration

$$x + \mathrm{i}y = \frac{1}{\delta} \frac{\rho \mathrm{e}^{\mathrm{i}\phi} + \gamma}{1 + \gamma \rho \mathrm{e}^{\mathrm{i}\phi}}, \tag{2.4}$$

with constants γ and β depending on the geometry through δ and e:

$$\gamma = \left\{ \left(\frac{2 + \delta(1 - e^2)}{2e} \right)^2 - 1 \right\}^{1/2} - \frac{2 + \delta(1 - e^2)}{2e} \quad \text{if } e \neq 0, \text{ else } \gamma = 0, \tag{2.5}$$

$$\beta = \frac{1 + \delta(1 + e) - \gamma}{1 - \gamma(1 + \delta(1 + e))}. \tag{2.6}$$

Unlike classical bipolar coordinates, this system is non-singular in the concentric limit, allowing computations in the axisymmetric case. Local orthogonality ensures separation of the variables in the expression of the Laplacian operator. An additional transformation maps the non-dimensional 'pseudo-radius' $1 \leqslant \rho \leqslant \beta$ to $-1 \leqslant \xi \leqslant 1$, with $\xi = (2\rho - \beta - 1)/(\beta - 1)$. In the local frame, the in-plane velocity is decomposed as $\boldsymbol{u}_\perp = u\boldsymbol{e}_\xi + v\boldsymbol{e}_\phi$. Expressions for operators in (2.2)–(2.3), written in the (ξ, ϕ) coordinate system, are given in the Appendix.

Linear stability theory predicts the behaviour of small-amplitude perturbations $\boldsymbol{X}'(\xi, \phi, z, t) \equiv (u', v', w', p')^t$ superimposed on the basic flow, $\boldsymbol{X}_B(\xi, \phi) \equiv (u_B, v_B, w_B, p_B)^t$. The system being homogeneous along the axial direction z, small perturbations can be written in normal-mode form:

$$\boldsymbol{X}'(\xi, \phi, z, t) = \boldsymbol{X}(\xi, \phi) \exp[\mathrm{i}(kz - \omega t)]. \tag{2.7}$$

As usual in temporal stability analyses, the axial wavenumber k is real, and the frequency is a complex number $\omega = \omega_r + \mathrm{i}\omega_i$. The phase speed $c \equiv \omega_r/k$ characterizes axial propagation, and the growth rate ω_i indicates temporal growth/decay (respectively, $\omega_i > 0$ and $\omega_i < 0$). Linearization of the Navier–Stokes equations about the basic flow and use of the normal-mode form (2.7) gives the system of differential equations $\boldsymbol{A}\boldsymbol{X} = \mathrm{i}\omega\boldsymbol{B}\boldsymbol{X}$, expressed in the (ξ, ϕ) coordinate system

as follows:

$$\boldsymbol{A} = \begin{bmatrix} A_{11} & A_{12} & 0 & D_\xi \\ A_{21} & A_{22} & 0 & D_\phi \\ D_\xi w_B & D_\phi w_B & A_{33} & \mathrm{i}k \\ D_\xi + A & D_\phi - B & \mathrm{i}k & 0 \end{bmatrix}, \quad \boldsymbol{B} = \begin{bmatrix} 1 & 0 & 0 & 0 \\ 0 & 1 & 0 & 0 \\ 0 & 0 & 1 & 0 \\ 0 & 0 & 0 & 0 \end{bmatrix}, \tag{2.8}$$

$$\left.\begin{aligned} A_{11} &= (u_B D_\xi + D_\xi u_B) + v_B(D_\phi - B) + \mathrm{i}k w_B - Re_\Omega^{-1}(\nabla_\perp^2 - k^2 + C), \\ A_{22} &= (v_B D_\phi + D_\phi v_B) + u_B(D_\xi + A) + \mathrm{i}k w_B - Re_\Omega^{-1}(\nabla_\perp^2 - k^2 + C), \\ A_{33} &= (u_B D_\xi + v_B D_\phi) + \mathrm{i}k w_B - Re_\Omega^{-1}(\nabla_\perp^2 - k^2), \\ A_{12} &= -2A v_B + (D_\phi - B)u_B + 2Re_\Omega^{-1}\left(AD_\phi + BD_\xi\right), \\ A_{21} &= 2B u_B + (D_\xi + A)v_B - 2Re_\Omega^{-1}\left(AD_\phi + BD_\xi\right). \end{aligned}\right\} \tag{2.9}$$

The symbols D_ξ, D_ϕ are differential operators given in the Appendix, together with the spatially dependent factors A, B and C. At the walls, impermeability $u = 0$, no-slip $v = w = 0$ and incompressibility $D_\xi u = 0$ conditions apply. For each value of k, the solution of this eigenvalue problem yields a spectrum of temporal modes $\omega = \Omega(k; \eta, e, Re_z, Re_\Omega)$. The critical azimuthal Reynolds number is such that the mode with the largest growth rate is at most neutrally stable ($\omega_{i,max} = 0$). The value of k for which it is neutrally stable is called the critical wavenumber.

The eigenvalue problem is invariant under complex conjugation (denoted by $\star$) $(k, \omega, \boldsymbol{X}) \mapsto (-k, -\omega^\star, \boldsymbol{X}^\star)$, so only $k > 0$ need be considered. In the absence of axial flow, the problem is also invariant to axial reflection, implying, with conjugation symmetry, that the spectrum is symmetric with respect to the imaginary axis ($\omega \mapsto -\omega^\star$). When axial flow is added, mirror symmetry of the system in the axial direction and the resulting symmetry of the spectrum are lost.

2.2. *Numerical method*

A spectral decomposition of the fields was implemented, as in Oikawa *et al.* (1989*a*) and Chawda & Avgousti (1996), using a Fourier–Chebyshev decomposition:

$$u(\xi, \phi) = \sum_{i=0}^{N_\xi - 1} \sum_{j=-K_\phi}^{K_\phi} \hat{\boldsymbol{u}}_{ij} \mathrm{e}^{\mathrm{i}j\phi} T_i(\xi), \tag{2.10}$$

where T_i is the Chebyshev polynomial of order i. A pseudospectral collocation method is used in the pseudo-radial direction, employing a Gauss–Lobatto distribution $\xi_i = \cos[i\pi/(N_\xi - 1)]$, with $0 \leqslant i \leqslant N_\xi - 1$. K_ϕ is the number of Fourier components, corresponding to $N_\phi = 2K_\phi + 1$ points on the physical grid (figure 1), after inverse discrete Fourier transform.

Steady solutions $\boldsymbol{u}_{B,\perp}$ of (2.2) are calculated using a time-marching procedure, then the axial flow w_B is obtained by solving the linear system (2.3). Thanks to the linearity of (2.3) with respect to w_B, the axial pressure gradient G is just a multiplying factor on the axial velocity, so G can be set to 1 without loss of generality. w_B is then rescaled to yield the required axial Reynolds number Re_z.

Integration of (2.2) is performed using a projection method enhanced with a preliminary pressure-prediction step (Goda 1979; Raspo *et al.* 2002). A simple and robust first-order temporal scheme is used since only steady solutions are of interest here. The stiff viscous terms of the vectorial Laplacian operator involving the scalar Laplacian $\nabla_\perp^2$ (see the Appendix) are treated implicitly, while all other terms are extrapolated from the previous time step. The Poisson and Helmholtz problems involve

block pentadiagonal matrices, and are efficiently solved using the Thomas algorithm. The choice of time step was automated in order to achieve convergence. When velocity residuals in the physical space $\max_{i,j}|u^n_{i,j}-u^{n-1}_{i,j}|$ or $\max_{i,j}|v^n_{i,j}-v^{n-1}_{i,j}|$ diverged, the time step was divided by 2: the resulting time steps ranged from 1 for the concentric case to 10^{-2} for $Re_\Omega = 250$, $e \geqslant 0.8$, and $N_\xi = K_\phi = 32$. The convergence tolerance on the residuals was set to 10^{-8}.

Approximating normal modes (2.7) with the same Fourier–Chebyshev expansion as the basic flow leads to a generalized eigenvalue problem, with matrix versions of linear operators (2.8)–(2.9), of size $4N_\phi N_\xi$. This generalized eigenvalue problem can be reduced to a standard eigenvalue problem $\widetilde{\boldsymbol{A}}\widetilde{\boldsymbol{X}} = \mathrm{i}\omega\widetilde{\boldsymbol{X}}$ of size $2N_\phi(N_\xi - 3)$, after eliminating w, p and boundary points of u and v. The reduction is performed numerically and allows significant time savings in full-spectrum calculation, as well as avoiding spurious eigenvalues. A similar approach seems to have been used in Oikawa *et al.* (1989*a*).

Full-spectrum computations were performed using the standard QR procedure available in the free software package LAPACK (www.netlib.org/lapack). When the region of interest in the spectrum was known beforehand, we used the Arnoldi (1951) method to compute a few eigenvalues efficiently. The shift–invert spectral transformation was used to enhance convergence, where the initial problem was replaced by $(\widetilde{\boldsymbol{A}} - \sigma\boldsymbol{I})^{-1}\widetilde{\boldsymbol{X}} = \nu\widetilde{\boldsymbol{X}}$. The eigenvalues $\nu = 1/(\lambda - \sigma)$ of largest magnitude give the corresponding eigenvalues $\lambda = \mathrm{i}\omega$ of the original problem closest to the given shift σ. The eigenvectors $\widetilde{\boldsymbol{X}}$ of the new problem are those of the initial one. The method requires solving linear systems involving the non-sparse matrix $\widetilde{\boldsymbol{A}} - \sigma\boldsymbol{I}$, which is factorized in LU form in an initialization step. The calculations were performed using the ARPACK++ class for non-sparse matrices (www.caam.rice.edu/software/ARPACK), based on LAPACK routines.

For a given mode, critical curves were calculated using a Newton–Raphson iteration: k and Re_Ω were varied simultaneously so as to reach $|\omega_i|$ and $|\partial_k\omega_i|$ less than 10^{-6}. Initial estimates for the critical k and Re_Ω were obtained by linear extrapolation with respect to Re_z. Identification of the most unstable modes is discussed in § 2.5.

2.3. *Spatial resolution*

A systematic grid refinement study was performed for the basic flow with $16 \leqslant N_\xi \leqslant 64$ and $0 \leqslant K_\phi \leqslant 128$ ($K_\phi = 0$ for $e = 0$), for $e \leqslant 0.99$ and $Re_\Omega \leqslant 250$. The minimal resolution achieving convergence of six significant digits of a number of integral quantities (forces and torque on inner cylinder, Fanning friction factor $f \equiv d|G|/(1/2\rho\overline{w}^2)$, azimuthal volume flux) was found for each set of parameters, and used for the computations in § 2.4. It appears that refining the number of collocation points much above $N_\xi = 32$ is unnecessary for $Re_\Omega \leqslant 250$, and the dependence on eccentricity is weak. On the other hand, if eccentricities close to 1 are considered, ϕ varies extremely slowly in the wide gap and a large number of Fourier modes is required. For $e = 0.98$ and $Re_\Omega = 223.61$, a resolution of $N_\xi \times K_\phi = 32 \times 128$ achieves excellent results, as can be seen in figure 2, which shows a comparison with Escudier *et al.* (2000)'s calculations.

In parametric stability analyses, however (§§ 3 and 4), a fixed resolution of $N_\xi = K_\phi = 16$ was systematically used for both basic-flow and normal modes, for practical reasons and because of the computational cost. Tests were performed *a posteriori* to check that these values provided reliable results, and are reported in table 1. With the chosen resolution, three significant digits of the critical Re_Ω are

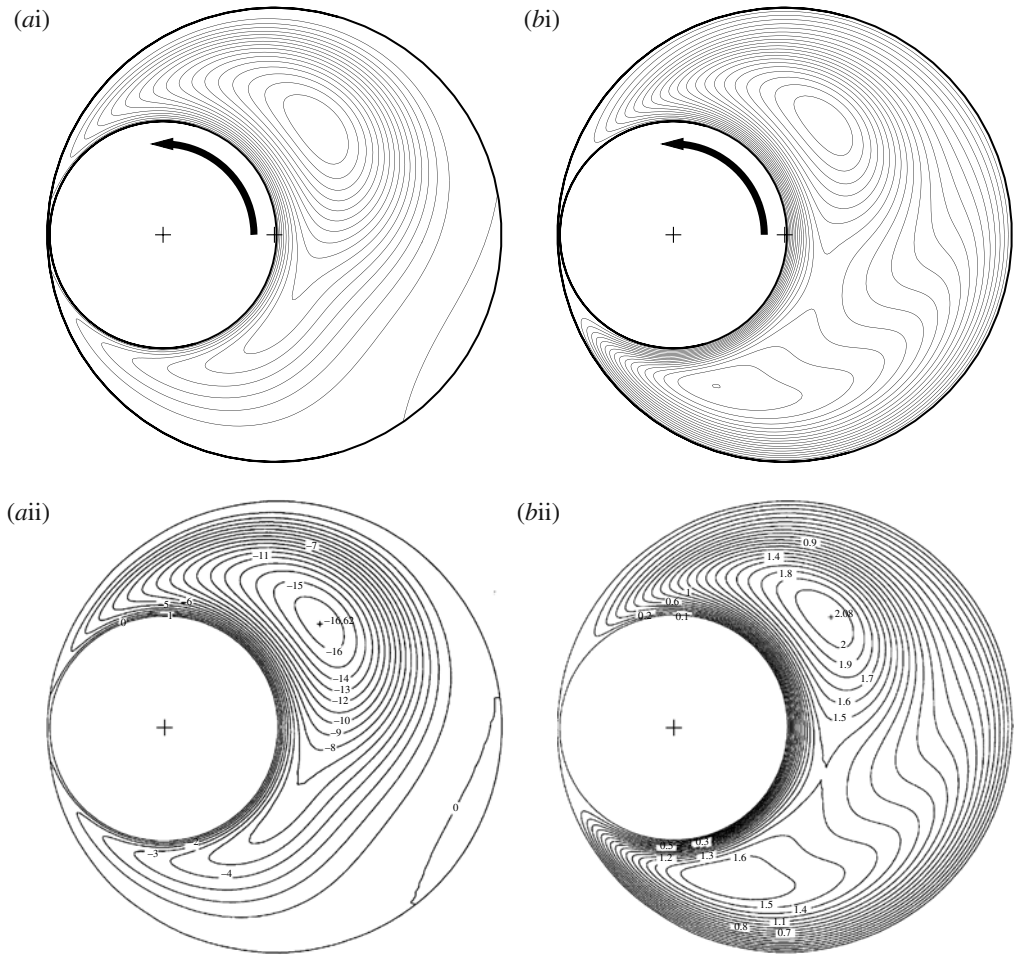

FIGURE 2. The basic flow for $\eta = 0.5$, $e = 0.98$ and $Re_\Omega = 223.61$: (i) the present calculation using $N_\xi \times N_\phi = 32 \times 257$ ($K_\phi = 128$); (ii) Escudier *et al.* (2000) with a 40×256 grid – (*a*) streamlines; (*b*) isolines of axial velocity normalized by mean velocity $\overline{w}$. The calculation recovers the secondary recirculation region in the wide gap and the two distorted maxima in the axial velocity. The numerical values of the isolines match those of Escudier *et al.* (2000).

converged in most cases. However, larger inaccuracies occur for high e and Re_z, and critical curves are truncated below $Re_\Omega = 200$ (respectively, $Re_\Omega = 250$) for $\eta = 0.5$ (respectively, $\eta = 0.89$), as remeshing above this limit quickly becomes prohibitive.

2.4. *Basic flow*

The most striking feature of the basic flow is the occurrence of a recirculation eddy for eccentricities larger than a certain threshold value of $\sim$0.3 for $\eta = 0.5$ (see figure 3), which only depends weakly on Re_Ω. This behaviour exists even for Stokes flow and Kamal (1966) was the first to study the influence of inertial effects. The recirculation is due to the adverse pressure gradient caused by the large expansion of annulus clearance, downstream of the 'bottleneck' at $\phi = \pi$. Figure 4(*d*) represents

	e	0.5				0.6				0.7			
	$N_\xi \times K_\phi$	16×16		32×32		16×16		32×32		16×16		32×32	
η	Re_z	Re_Ω	k	Re_Ω	k	Re_Ω	k	Re_Ω	k	Re_Ω	k	Re_Ω	k
0.5	50	127.41	3.34	127.41	3.35	147.52	3.45	147.52	3.45	184.99	4.26	185.13	4.23
	100	151.61	3.17	151.63	3.17	171.59	2.67	171.76	2.69	212.78	3.21	213.19	3.20
	150	156.73	2.86	156.76	2.86	187.61	2.76	188.25	2.76	231.15	2.57	230.28	2.77
	180	156.91	2.78	157.02	2.79	191.58	2.53	191.94	2.58	238.15	2.94	243.96	3.02
	200	156.15	2.53	156.28	2.54	194.73	2.42	193.98	2.49	237.85	2.74	246.89	2.91
0.8907	32	247.82	2.98	247.82	2.98	—	—	—	—	—	—	—	—
	50	296.19	2.74	296.20	2.74	—	—	—	—	—	—	—	—
	17	—	—	—	—	247.40	3.40	247.46	3.40	—	—	—	—
	30	—	—	—	—	283.26	3.11	284.04	3.13	—	—	—	—

TABLE 1. Resolution tests for $\eta = 0.5$ and $\eta = 0.8907$, with $N_\xi \times K_\phi = 16 \times 16, 32 \times 32$. Critical Re_Ω and k are given for various e and Re_z.

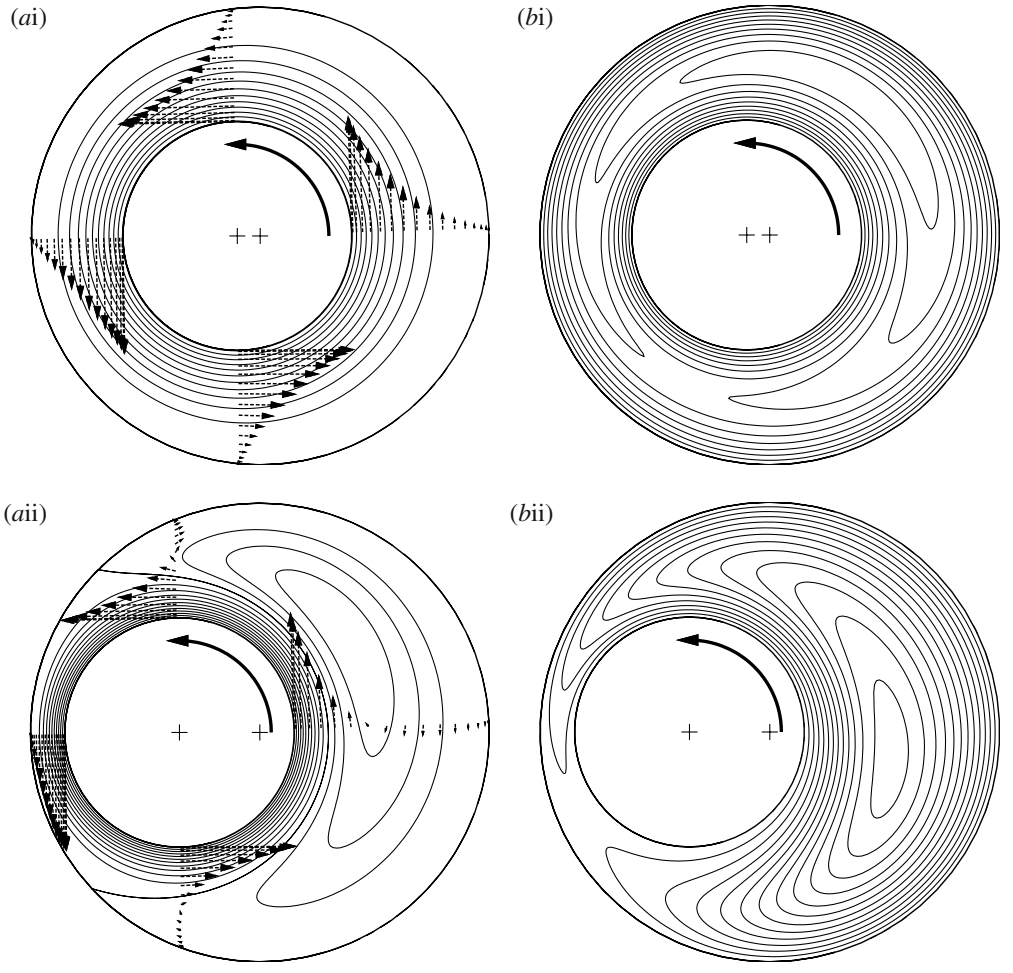

FIGURE 3. Basic flows for $\eta = 0.5$, $Re_\Omega = 100$: (i) weak eccentricity $e = 0.2$; (ii) high eccentricity $e = 0.7$ – (a) contours of equispaced in-plane streamfunction with superimposed in-plane velocity profiles at $\theta = 0, \pi/2, \pi, 3\pi/2$ (polar angle with respect to the inner cylinder); (b) equispaced contours of axial velocity.

the evolution of the azimuthal volume flux (per unit length) Q_ϕ with eccentricity, for $\eta = 0.5$ and azimuthal Reynolds numbers Re_Ω up to 250. Q_ϕ is obtained by integration of the azimuthal velocity along the radial path $\phi = 0$ joining the cylinders. As the inner cylinder gets closer to the outer one, the azimuthal flow becomes progressively 'choked', and Q_ϕ seems to be controlled by the smaller gap width. Indeed, the flow in the vicinity of the inner cylinder resembles a circular Couette flow of clearance ratio controlled by the smaller gap, while the wide-gap region hosts a low-velocity recirculation zone contributing no net azimuthal volume flux. A comparison is made with the value of Q_ϕ in the Stokes régime, using Wannier (1950)'s exact formula for the in-plane stream function. Inertial effects only have a weak impact on Q_ϕ, which could be expected from the fact that the fluid is entrained in rotation by viscous forces.

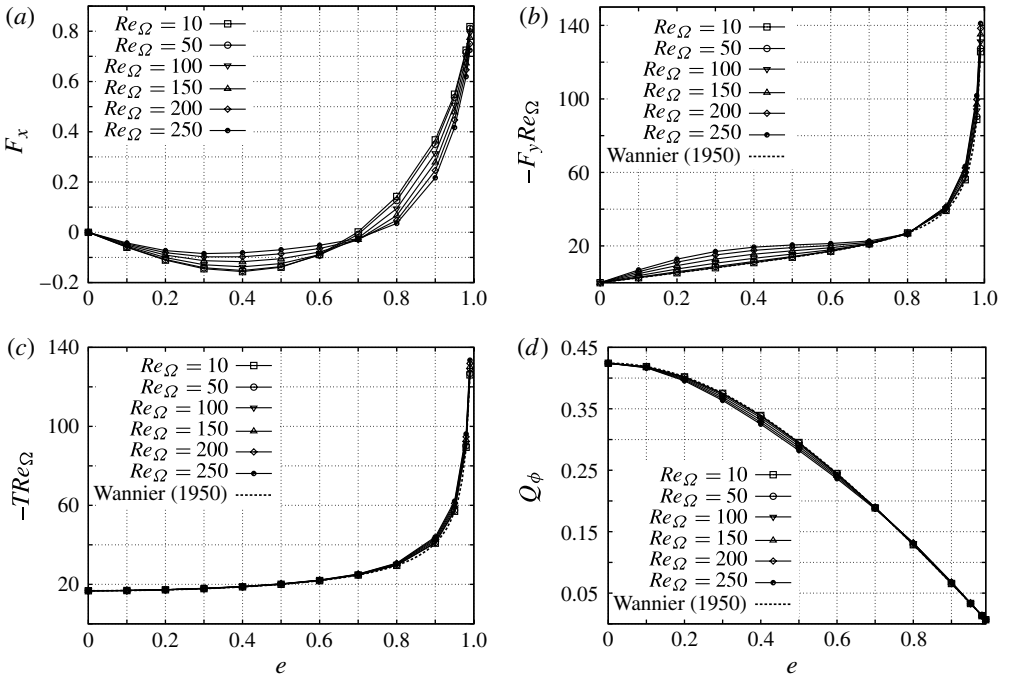

FIGURE 4. The forces, torque and azimuthal flow rate (per unit length) for $e = 0, \ldots, 0.7$ and $Re_\Omega = 10, \ldots, 250$: (*a*) the *x*-component F_x; (*b*) the *y*-component F_y of the force on the inner cylinder; (*c*) the torque T on the inner cylinder; (*d*) the azimuthal flow rate Q_ϕ. The dotted lines in (*b–d*) correspond to the exact value in the Stokes régime, taken from Wannier (1950).

Maximum axial velocity occurs in the wide-gap region. Indeed, in the absence of rotation, eccentric annular Poiseuille flow is nearly parabolic in the pseudo-radial direction, and for any fixed value of ϕ, the maximum velocity scales as the 'local clearance' squared. However, the position of the maximum axial velocity is not exactly located at $\phi = 0$, because of convective transport of w_B by cross-flow components $\boldsymbol{u}_{B,\perp}$ (see (2.3)). In fact, these nonlinear effects distort the whole flow field, and Escudier *et al.* (2000) performed a thorough computational/experimental analysis of the effects of eccentricity and inner-cylinder rotation, on annular Poiseuille flow. At low eccentricity, the maximum axial velocity was shown to be advected towards the narrowing-gap region, inducing a slight increase in Fanning friction factor (defined in § 2.3) with e. For moderate eccentricities $0.3 \leqslant e \leqslant 0.8$, the maximum moves back to the wide-gap region, with a subsequent decrease in friction factor. For larger eccentricities, the maximum is located in the diverging-gap region, and the friction factor increases again. At very high eccentricities and rotation rates, a second peak in axial velocity appears in the wide gap, while a secondary recirculation is observed at the outer cylinder wall. This complex pattern is successfully obtained with our code, as illustrated in figure 2.

The forces on the inner cylinder can be easily computed by integration of the pressure and viscous stresses at the wall. The expressions for the strain tensor components in our coordinate system are given in the Appendix. Figure 4 shows a systematic study of the effect of Re_Ω and e on the loads, for $\eta = 0.5$. A comparison is made with the Stokes régime, using analytical formulas derived by Wannier (1950). In

this limit, the velocity and pressure distributions are antisymmetric with respect to the symmetry plane of the annulus. Therefore, the x-component of the force is exactly 0. At the inner-cylinder surface, the pressure increases with ϕ on the wide-gap side up to $0 < \phi_{max} < \pi$, and decreases on the small-gap side up to $\phi_{min} = -\phi_{max}$. As e increases, the pressure extrema both tend to the same limit $\phi_{min/max} \to \pi$. Because $0 < \phi_{max} < \pi$, the y-component of the force F_y is negative. The viscous torque T is obviously opposed to the sense of rotation, so $T < 0$. In the Stokes limit, T and F_y both scale as Re_Ω^{-1}. Indeed, the torque T is induced by shear stresses τ, which scale as $\tau \sim \mu V/L$ in dimensional form, where μ is the dynamic viscosity. Non-dimensionalizing with respect to the pressure scale $P \equiv \rho V^2$, one obtains $T \sim \tau \sim Re_\Omega^{-1}$. In the absence of inertial terms, the pressure p_B also scales as τ, so $F_y \sim p_B \sim \tau \sim Re_\Omega^{-1}$.

When inertial effects are added, this scaling still holds and only small deviations to the Stokes limit are observed. Larger variations occur for an eccentricity of ~0.3–0.4, where the value of $F_y Re_\Omega$ at $Re_\Omega = 250$ is almost twice the purely viscous one. At $e \approx 0.8$, variations of $F_y Re_\Omega$ with Re_Ω are almost non-existent. Similarly, the formula for the torque in the Stokes régime applies quite robustly for all the range of eccentricities and Re_Ω up to 250. Again, this close agreement is attributed to the fact that the flow in the vicinity of the inner cylinder is similar to a circular Couette flow where inertial effects are weak (and non-existent in the purely axisymmetric case). For e close to 1, F_y and T increase sharply because of lubrication effects.

When $Re_\Omega \neq 0$, the flow antisymmetry is broken, and F_x is non-zero. For low eccentricities, F_x is negative, but for high e, F_x is positive, as expected from lubrication theory. The change of sign of F_x is located about a critical eccentricity of $e \approx 0.7$–0.75 for $\eta = 0.5$ and $Re_\Omega \leqslant 250$, as already discussed by Feng *et al.* (2007) and Podryabinkin & Rudyak (2011). Small-eccentricity perturbations about this point tend to push the inner cylinder back to its initial position. However, pressure-induced precession prevents any stable equilibrium for this value of eccentricity, explaining the complex motion of drillstrings in wellbores. The intensity of F_x is determined by the magnitude of the convective term, so the pressure scaling $P \equiv \rho V^2$ is appropriate in this case.

2.5. *Critical modes*

The first step in linear stability analysis is to identify a reduced set of leading modes, with the largest growth rates. Full-spectrum computations were used to find the most unstable eigenvalue at each point of a coarse grid in (e, Re_Ω, Re_z), for $\eta = 0.5$. k was varied between 1 and 7, a range containing all the critical wavenumbers for the concentric case with $Re_z \leqslant 200$ ($1.5 \lesssim k \lesssim 4.5$ from the graph in Cotrell & Pearlstein 2004), with large steps of 0.5 for computational efficiency. Approximate critical curves were obtained, and it was found that the modes at criticality are always either propagating 'Taylor-like' vortices or deformed left-handed helical modes. These pseudo-toroidal and pseudo-helical modes correspond to the same family of critical modes found in Taylor–Couette–Poiseuille flow (Takeuchi & Jankowski 1981), but distorted by eccentricity (cf. figure 10). In the axisymmetric case, these modes can be assigned an integer azimuthal wavenumber m corresponding to a normal-mode decomposition of the form $\boldsymbol{X}' = \boldsymbol{X}(r)\exp[\mathrm{i}(kz + m\theta - \omega t)]$, using the usual cylindrical coordinates (r, θ, z). Considering $k > 0$, $m = 0$ correspond to Taylor vortices and $m > 0$ (respectively, $m < 0$) are left-handed (respectively, right-handed) helical vortices, with helicity opposed to (respectively, matching) that of the basic flow. Following these modes by continuity, pseudo-helices are also assigned a 'pseudo-azimuthal wavenumber' equal to the corresponding value of m in the concentric case. Henceforth,

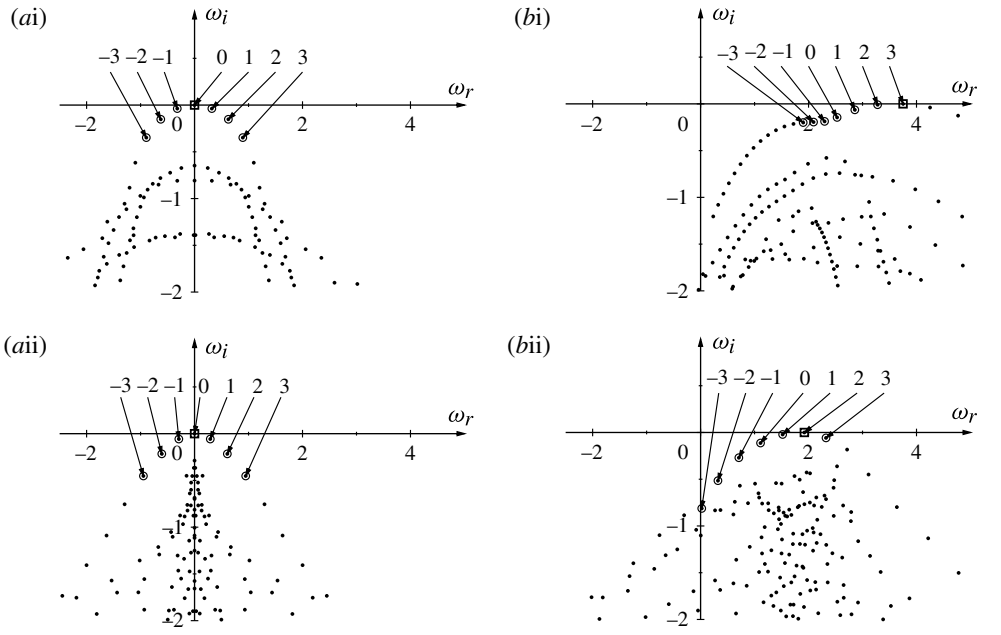

FIGURE 5. Spectra of eigenvalues $\omega = \Omega(k; e, Re_\Omega, Re_z)$ with (k, Re_Ω) at critical conditions. Rows: (i) $e = 0$; (ii) $e = 0.5$. Columns: (*a*) $Re_z = 0$; (*b*) $Re_z = 50$. Numbers indicate the azimuthal wavenumber m of the eigenmode (or pseudo-wavenumber if eccentric). Positive ω_i indicates instability. Positive (negative) m correspond to left- (right-)handed helix-like modes. The eigenvalue in the square box corresponds to the most unstable mode.

TV will denote 'Taylor-like' vortices, while LH$|m|$ and RH$|m|$ will correspond to left-handed (respectively, right-handed) helical vortices of order m. The symmetry of the spectrum for $Re_z = 0$ implies that LH and RH of equal order m have the same growth rate and oppositely signed phase speeds. As Re_z is increased, LH modes become more unstable than TV and RH, and form the family of critical modes, as in the axisymmetric case (cf. figure 5). The critical value of m increases steadily with Re_z.

Additional families of modes, such as wall modes related to a shear instability mechanism, were not found to be critically unstable in the range of parameters considered. Centre modes of *Sp* type, such as described by Merzari *et al.* (2008), and critical in highly eccentric annular Poiseuille flow for high values of Re_z, were not found to be critical in our configuration either.

In axisymmetric Taylor–Couette–Poiseuille flow with $\eta = 0.5$, the maximum value of m at criticality is 7 (Cotrell & Pearlstein 2004). Hence, in the subsequent parametric study at $\eta = 0.5$ (§ 3), critical curves were calculated for TV, LH modes with $m \leqslant 7$, and RH of order one and two, as a check.

2.6. *Validation*

Extensive validations of basic-flow and stability calculations have been performed. In the Stokes limit $Re_\Omega \ll 1$, Wannier (1950) derived analytical expressions for torque and forces on the inner cylinder, that were matched by our code up to machine precision. Using his analytical solution of the stream function, azimuthal volume flux Q_ϕ calculations were also successfully validated. Escudier *et al.* (2000) calculated

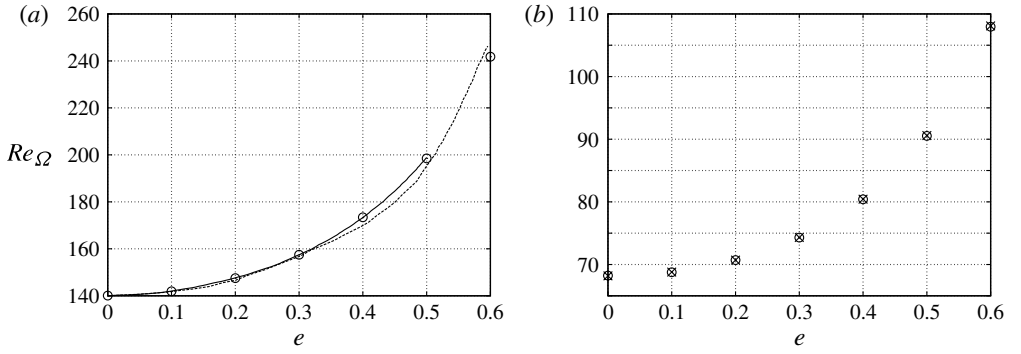

FIGURE 6. Validation of critical azimuthal Reynolds number Re_Ω against eccentricity e. (a) $\eta = 0.912$, $k = 3.17$: solid line, Chawda & Avgousti (1996); dotted line, Dai *et al.* (1992), ∘, present calculation. (b) $\eta = 0.5$: ×, Oikawa *et al.* (1989*a*); ∘, present calculation.

the Fanning friction factor (defined in § 2.3) in the eccentric Taylor–Couette flow, for $10 \leqslant Re_\Omega \leqslant 223.61$ and eccentricities up to 0.98. The present numerical results all lay within 0.67 % of their values. Feng *et al.* (2007) gave numerical values for the pressure and stress contributions to the x and y components of the force on the inner cylinder for $Re_\Omega = 125$ and eccentricities up to $e = 0.98$. For these parameters, our calculations match their results, with less than 1.80 % of relative difference, and 0.76 % on average when at least four significant digits were provided by the authors.

In the axisymmetric configuration with axial throughflow, Takeuchi & Jankowski (1981) performed the first numerical prediction of the critical curves for Re_z up to 100. In their paper, they provide data for the critical values of Re_Ω, k and wave speed $c = \omega_r/k$ for $Re_z = 0, 10, \ldots, 100$. The critical values are exactly matched by our code in all cases except for $Re_z = 90$, where only the last significant digit given by the authors for k and c differs from our values by one.

In the eccentric configuration with no axial flow, Oikawa *et al.* (1989*a*) reported a critical azimuthal Reynolds number of 307.59 for an axial wavenumber of 4.126 and $\delta = 0.1$, $e = 0.7$. With the same spatial resolution $N_\xi \times K_\phi = 21 \times 24$, our corresponding critical values are $Re_\Omega = 307.71$ and $k = 4.127$, which gives relative errors of 0.04 and 0.02 %, respectively. Additional tests were performed using a graph of critical Re_Ω versus eccentricity for $\eta = 0.5$ from a second paper of Oikawa *et al.* (1989*b*), and for $\eta = 0.912$ and $k = 3.17$ against graphical results from Dai *et al.* (1992) and Chawda & Avgousti (1996). Figure 6 shows excellent agreement with the data of Oikawa *et al.* (1989*b*) and Chawda & Avgousti (1996), who both used the same spectral decomposition of the modes as us. Values from Dai *et al.* (1992) are close, but discrepancies may be attributed to their relatively coarse meshing ($N_\phi = 16$ points only in the 'pseudo-azimuthal' direction) and to the use of piecewise polynomials to approximate the fully nonlinear fields in their bifurcation analysis.

3. Parametric study for a wide gap $\eta = 0.5$

In this section, we give results for the case $\eta = 0.5$, representative of industrial configurations in oil-well drilling. A resolution of $N_\xi = K_\phi = 16$ allows satisfactory accuracy for $e \leqslant 0.7$ and Re_Ω, Re_z up to 200, as shown in the previous section.

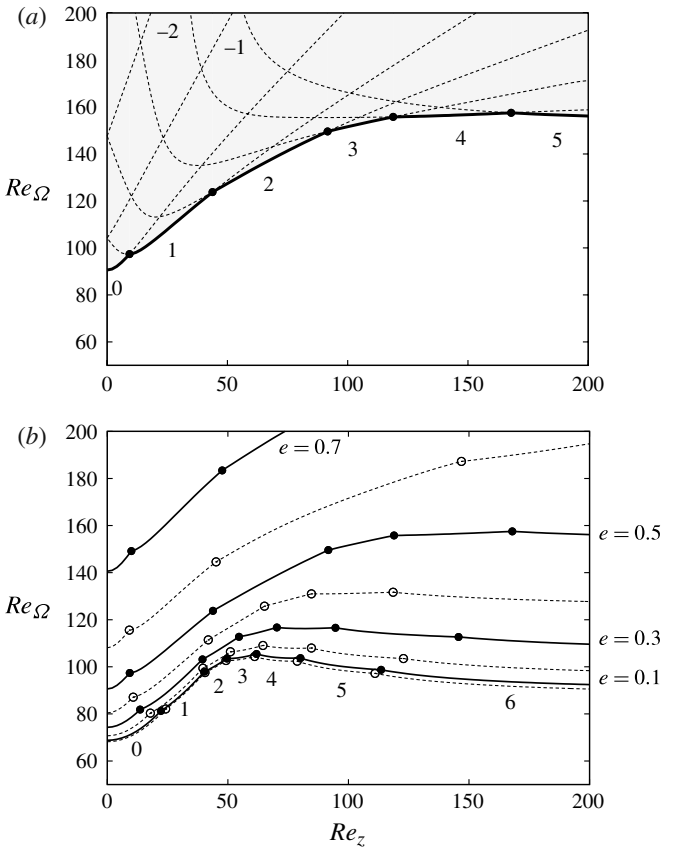

FIGURE 7. (*a*) Critical curves $Re_\Omega = f(Re_z)$ for $e = 0.5$ and modes $m = -2, \ldots, 5$. The thick solid line indicates the instability threshold taking all the modes into account. The shaded area corresponds to instability. (*b*) Solid (respectively, dotted) lines: critical curves taking all the modes into account, for $e = 0.1, 0.3, 0.5, 0.7$ (respectively, $e = 0, 0.2, 0.4, 0.6$). In both (*a*) and (*b*), filled/open circles indicate a switch in critical m, and the associated 'pseudo-azimuthal' wavenumber is indicated by annotation.

3.1. *Critical azimuthal Reynolds number*

For an eccentricity of $e = 0.5$, figure 7(*a*) shows the critical curves of the TV ($m = 0$), LH ($m > 0$) and RH ($m < 0$) modes labelled from $m = -2$ to 5. The solid thick line indicates the stability boundary, switching from one m to the next as Re_z is increased. Similar behaviour was found in the axisymmetric case by Takeuchi & Jankowski (1981).

Similar results were obtained for all eccentricities and figure 7(*b*) superimposes on a single figure all the results concerning the stability boundary for $e = 0, 0.1, \ldots, 0.7$. The main result of this study is clear from this figure: eccentricity always has a stabilizing effect, regardless of axial advection. The origin of this stabilization, as hinted at by Karasudani (1987) for the eccentric Taylor–Couette flow without axial flow, seems to lie in the weakening of centrifugal effects by eccentricity. Indeed, as already mentioned in § 2.4, azimuthal flow gets 'choked' with increasing eccentricity (see Q_ϕ in figure 4*d*), and the basic flow becomes similar to an axisymmetric Couette flow of clearance ratio δ', controlled by the small gap $\delta' \sim \delta(1 - e)$, next to a 'dead'

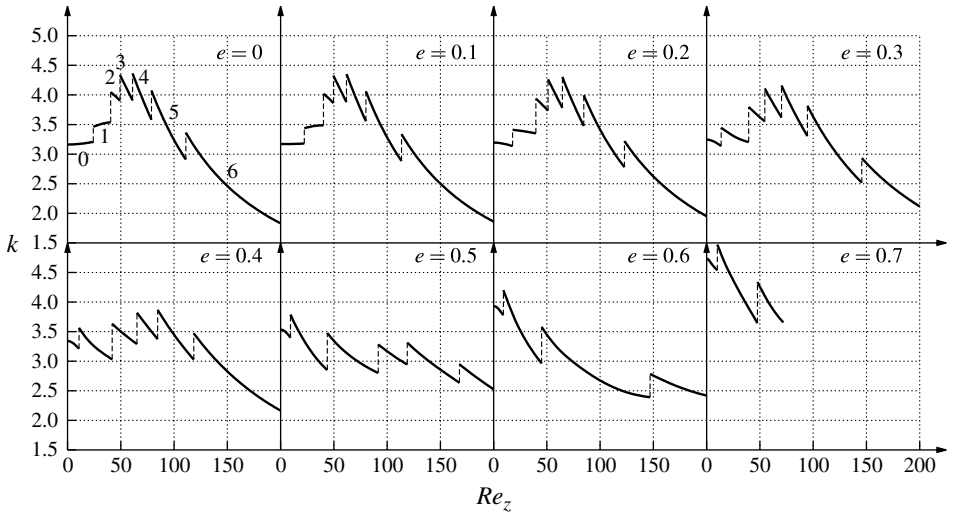

FIGURE 8. The critical wavenumber k against the axial Reynolds number Re_z for eccentricities $e = 0, 0.1, \ldots, 0.7$. Discontinuities correspond to a switch in critical m (values indicated by annotation for $e = 0$).

recirculating flow zone. Decreasing the clearance ratio or, equivalently, increasing the radius ratio of a circular Couette flow, reduces curvature effects and has a stabilizing effect, as shown by DiPrima, Eagles & Ng (1984).

The effect of axial advection on the axisymmetric case is twofold: first, it stabilizes the Couette flow up to $Re_z = 61.08$; and then it slightly destabilizes it as Re_z is further increased, while maintaining the threshold above the value for $Re_z = 0$. The change in behaviour corresponds exactly to the intersection between the increasing critical curve corresponding to mode $m = 3$ and the decreasing curve for $m = 4$; hence maximal stability is achieved when the two modes exchange stability. The value of Re_z corresponding to the maximum in critical Re_Ω increases with eccentricity. Above $e = 0.5$, maximum stability occurs beyond $Re_z = 200$.

At fixed Re_z above 50, increasing eccentricity tends to select critical modes of lower m: the stabilizing effect of eccentricity is even more important for higher azimuthal wavenumbers. On the contrary, at small Re_z, eccentricity favours the dominance of the LH1 over TV. For large enough eccentricities, one can expect helices with $m = 1$ to dominate TV even without axial flow. In the absence of axial flow, this feature was found experimentally by Vohr (1968) ($\delta = 0.099$ and $e > 0.707$) and Karasudani (1987) ($\eta = 0.83$, $e > 0.6$). Oikawa *et al.* (1989*a*) found a complex conjugate pair of eigenvalues $\lambda = \mathrm{i}\omega$ at criticality for $\delta = 0.1$, $e = 0.7$ (LH and RH), confirming numerically Vohr (1968)'s findings.

3.2. *Critical axial wavenumber*

Figure 8 shows the evolution of the critical wavenumber. The curves display jumps at points where modes exchange stability, and these discontinuities always correspond to a positive jump in k. When axial flow is increased, k usually decreases as long as the critical mode does not switch. The order of magnitude of k is always the same regardless of eccentricity, and remains between 1.5 and 5, which indicates that the axial wavelength of the critical perturbations is always of the same order of magnitude

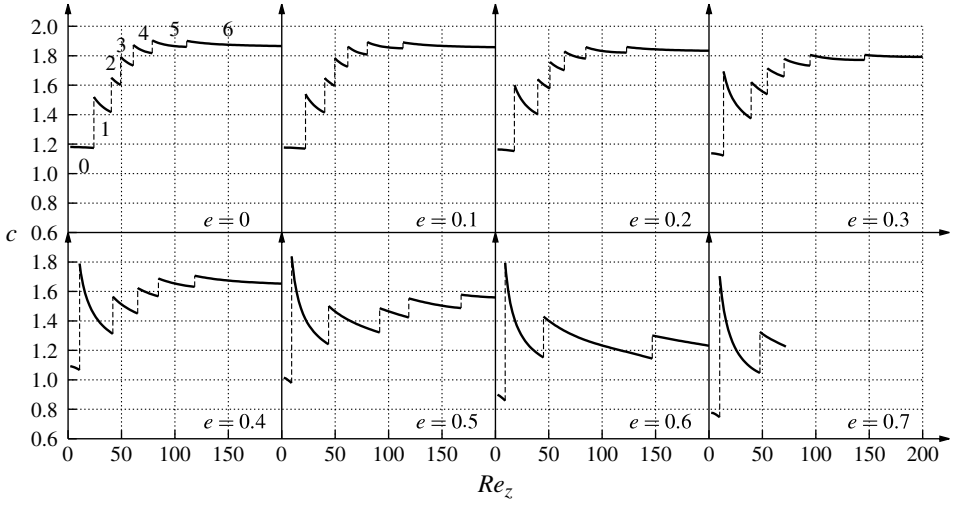

FIGURE 9. The critical phase speed c against the axial Reynolds number Re_z at critical conditions for eccentricities $e = 0, 0.1, \ldots, 0.7$. Discontinuities correspond to a switch in m (values indicated by annotation for $e = 0$). The unit is the average axial basic-flow velocity $\overline{w_B}$.

as the clearance $d = b - a$. These observations may explain the pattern selection process: increasing Re_z tends to elongate the modes in the axial direction, so a switch to a higher 'pseudo-azimuthal' wavenumber mode occurs to reach a vortical structure that fits the annular domain better, and is thus amplified faster.

3.3. *Critical phase speed*

Figure 9 shows the evolution of the phase speed at criticality. As in figure 8, the curves are discontinuous as critical m switches with increasing Re_z. The phase speed always remains between 0.6 times and twice the average axial velocity of the basic flow. It decreases with increasing Re_z for each mode, but discontinuities always correspond to a jump to a larger value. Interestingly, except for LH1 (LH with $m = 1$) at the point of stability exchange with TV, all the critical modes see their phase speed decrease with eccentricity, this effect being more noticeable for $e \geqslant 0.3$. Most critical perturbations propagate somewhat faster than the average axial flow velocity, but see their propagation hindered by increasing Re_z.

3.4. *Critical eigenmodes structure*

A systematic study of the spatial structure of the critical eigenmodes has been performed. Figure 10 shows a deformed LH1 for $e = 0.5$, $Re_z = 40$. Figure 10(*e*) clearly represents the helical structure, while figure 10(*b*) shows the $m = 1$ azimuthal order. In-plane motion of the mode (figure 10*a*) can be quite complicated and difficult to interpret for higher-order modes.

It is interesting to look at the disturbance kinetic energy distribution to see where the mode localizes within the annulus. Figure 10(*c*) shows concentration of the energy in the converging gap region, consistent with observations of Oikawa for TV perturbations in both the small- and wide-gap eccentric Taylor–Couette flow (and the numerous theoretical and experimental studies cited in the introduction, either calculating or observing the so-called 'maximum vortex activity' in the saturated

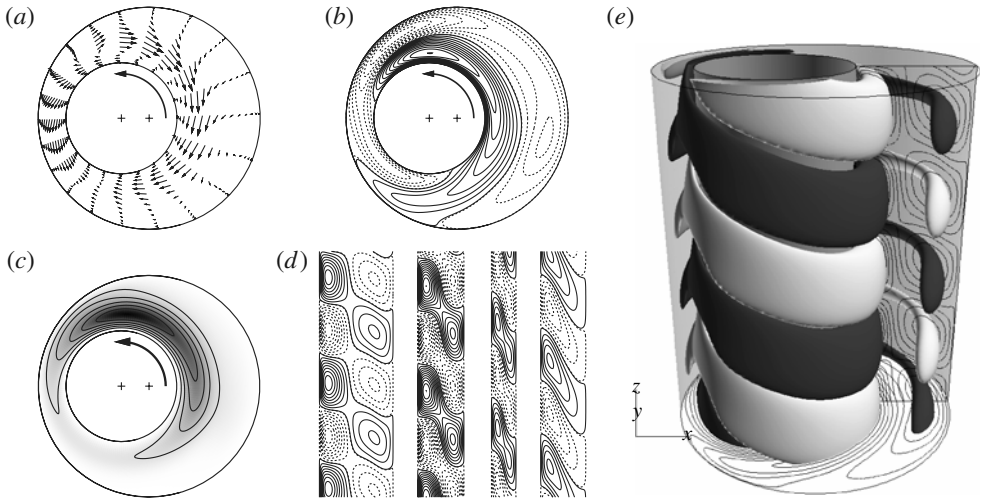

FIGURE 10. The structure of the critical eigenmode for $e = 0.5$, $Re_z = 40$. (*a*) The real part of the in-plane perturbation velocity $\boldsymbol{u}_\perp = (u, v)$. (*b*) Equispaced contours of the real part of the axial perturbation velocity w: solid (dotted) lines indicate positive (negative) values. (*c*) Map and (equispaced) contours of the disturbance energy density $\frac{1}{2}(|u|^2 + |v|^2 + |w|^2)$ dark grey corresponds to high values. (*d*) Vertical cuts (equispaced contours) of the real part of the axial perturbation velocity w for $\theta = 0, \pi/2, \pi, 3\pi/2$ (from left to right) in a polar coordinate system centred on the inner cylinder. (*e*) Isosurfaces of Re(w), showing the three-dimensional structure of the mode: dark (light) shades of grey indicate positive (negative) values, respectively.

régime). It is also possible to track the position of the maximum of the total disturbance energy. It is found that both in the axisymmetric and the $e = 0.5$ cases, the perturbation localizes closer and closer to the inner wall as advection is increased, at a radius (with respect to the inner cylinder) of $\sim$1.2–1.5 times the inner-cylinder radius. In the eccentric case, this maximum also moves azimuthally to the small-gap region, with jumps as the critical mode switches. At $Re_z = 0$ ($m = 0$), it is located at a polar angle (centred on the inner cylinder) of $\theta = 79°$, while at $Re_z = 200$ ($m = 5$), it is at $\theta = 121°$. From the energy density maps, it is also clear that as Re_z is increased, the energy is less and less spread out in the annular region and peaks around some radial position. For $Re_z = 0$, the ratio between the maximum of the total disturbance energy and the average is 5.7, whereas it is 16.3 for $Re_z = 200$.

Let us define the in-plane and axial disturbance energy contributions of a mode as the integral quantities over the annular domain $\mathscr{A}$:

$$E_\perp = \frac{1}{2}\int_{\mathscr{A}} (|u|^2 + |v|^2)\,\mathrm{d}\mathscr{A}, \quad E_z = \frac{1}{2}\int_{\mathscr{A}} |w|^2\,\mathrm{d}\mathscr{A}. \tag{3.1}$$

Figure 11 shows the contributions to the total disturbance energy of the critical mode as a function of Re_z for $e = 0$ and $e = 0.5$. In both cases, the graphs show how the energy transfers from dominantly in-plane motion to dominantly axial motion as advection is increased, regardless of the ('pseudo-')azimuthal wavenumber involved. There is a tendency for the modes to become more and more two-dimensional with suppressed spanwise (here azimuthal) motion, as for TS waves on a flat plate or in channel flow. This suggests that viscosity plays an important role in the destabilization

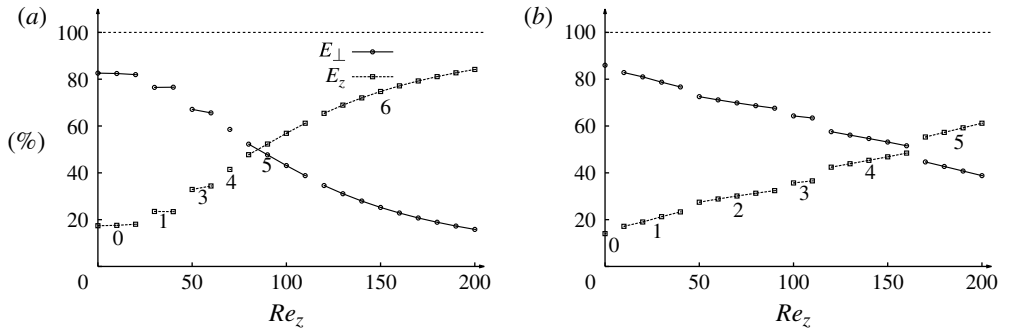

FIGURE 11. In-plane $E_\perp$ and axial E_z contributions to the total disturbance energy of the critical mode as a function of Re_z: (*a*) $e = 0$; (*b*) $e = 0.5$. Numbers indicate the ('pseudo')azimuthal wavenumber of the critical mode.

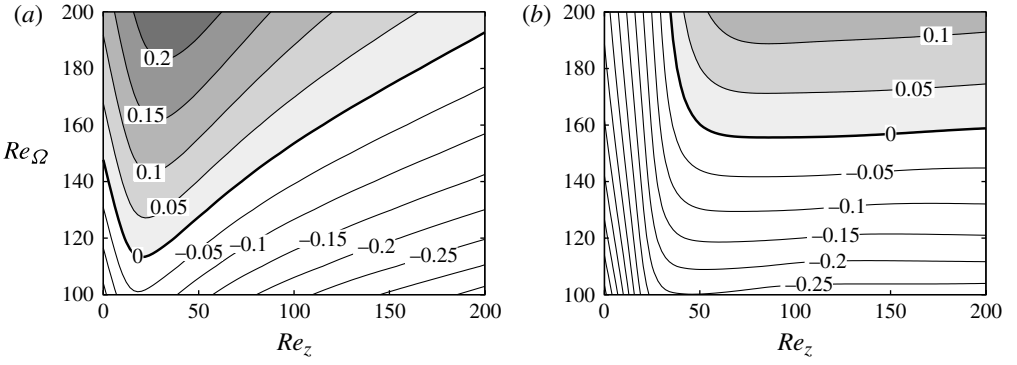

FIGURE 12. Growth rate maps for an eccentricity of $e = 0.5$: (*a*) mode $m = 2$; (*b*) mode $m = 4$.

of the modes at high Re_z. This hypothesis is consistent with the fact that the modes localize more and more in high-shear regions: closer to the inner wall at smaller clearance. It is also consistent with the decrease in critical axial wavenumber k with increasing Re_z (figure 8). Interestingly, in the case $e = 0.5$, the critical axial Reynolds number above which advection becomes destabilizing corresponds to the switch from dominantly in-plane disturbance energy to dominantly axial disturbance energy (this is less clear for $e = 0$). Note, however, that these modes are distinct from the 'pure' viscous wall modes referred to as modes A in Merzari *et al.* (2008) for eccentric Poiseuille flow, or TS-like modes in axisymmetric Taylor–Couette–Poiseuille flow (Cotrell & Pearlstein 2004). Those latter modes are localized about critical layers, and are expected to become critical at higher values of Re_z, typically of the order of 10^4 in the axisymmetric Taylor–Couette–Poiseuille flow with $\eta = 0.5$ (Cotrell & Pearlstein 2004).

3.5. *Growth rate maps and stability diagrams*

In the concentric and $e = 0.5$ cases, a more complete study of the dispersion relation was carried out. Figure 12 shows maps of the maximum growth rate $\omega_{i,max}$ in the (Re_Ω, Re_z) space for modes 2 and 4 and $e = 0.5$. For 'higher-order' modes such

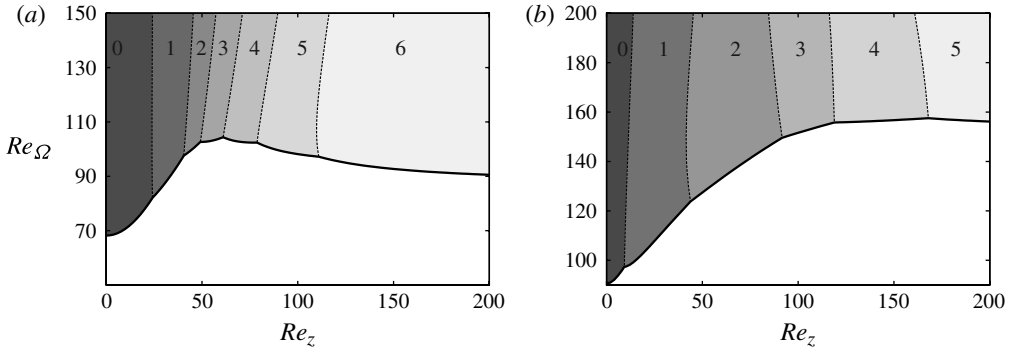

FIGURE 13. Dominant unstable modes in (Re_z, Re_Ω) space with and without eccentricity: (*a*) $e = 0$; (*b*) $e = 0.5$. Numbers indicate the azimuthal or 'pseudo-azimuthal' wavenumber of the fastest growing mode.

as $m = 4$, one can clearly distinguish two zones. For low Re_z, there is a sharp increase in $\omega_{i,max}$ with advection and rotation has only a minor effect on stability. For higher axial flow rates, the tendency is reversed: advection has only a weak effect on stability and centrifugal effects govern the stability of the mode. This trend was also observed in the concentric case for high-order left helices. For 'low-order' modes such as $m = 2$, the separation of the two effects is less clear: the increase of $\omega_{i,max}$ for weak axial advection is also observed, though less markedly, and at higher axial flow rates, the stabilizing effect of advection is comparable in magnitude to the destabilizing effect of rotation.

It is also possible to calculate the regions in which each m dominates the instability, as shown in figure 13. In the cases of both no eccentricity and of $e = 0.5$, it appears that frontiers between these regions are always close to straight lines parallel to the Re_Ω-axis. This again illustrates the importance of advection in the destabilization of the helical modes. While the instability mechanism is centrifugal in nature, there is a need for a minimum axial flow rate for this instability to operate on higher-order LH modes.

This importance of both shear and centrifugal effects in the destabilization process at high Re_z as noticed here and in the preceding subsection, is not a complete surprise. Indeed, as pointed out in Meseguer & Marques (2002), Hagen–Poiseuille flow is linearly stable for any Re_z; however, a slow rotation may destabilize the basic flow (Mackrodt 1976). Conversely, rigid-body rotation is linearly stable for any rotation rate, but the superposition of axial flow can also destabilize the flow. The same mechanism was observed for an axisymmetric Couette flow (Meseguer & Marques 2000) with axial motion of the inner cylinder, where both shear and centrifugal effects were needed to make the basic flow unstable. It is clear from figure 12(*b*) that here this is the case for higher-order helical modes: the region of instability is bounded by a threshold in both rotation and advection rates.

4. Parametric study for a small gap $\eta = 0.89$

As mentioned in the introduction, very little work has been done on the experimental study of eccentric Taylor–Couette–Poiseuille flow. However, some experimental data are available for radius ratios close to $\eta = 0.9$. We study the case $\eta = 0.89$ ($\eta = 0.8907$ to be exact), corresponding to the sharp entry apparatus in

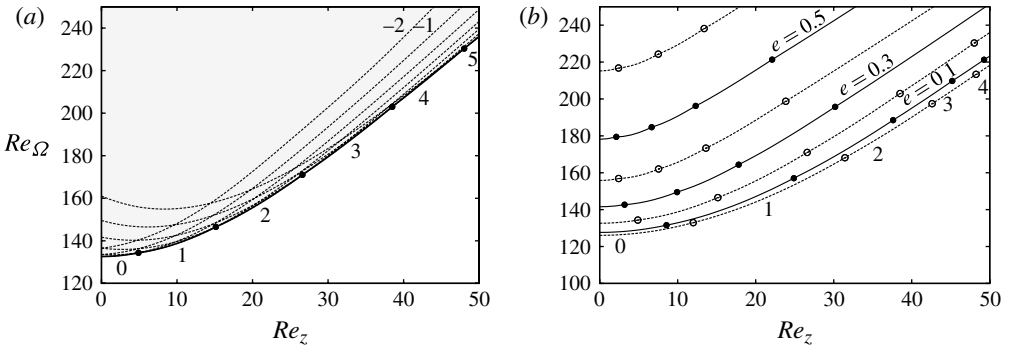

FIGURE 14. (*a*) Critical curves $Re_\Omega = f(Re_z)$ for $\eta = 0.8907$, $e = 0.2$ and modes $m = -2, \ldots, 5$: the thick solid line indicates the instability threshold taking all the modes into account; the shaded area corresponds to instability. (*b*) Critical curves taking all the modes into account, for different eccentricities $e = 0, 0.1, \ldots, 0.6$ and $\eta = 0.8907$. In both (*a*) and (*b*), dots indicate a switch in critical m, and the associated 'pseudo-azimuthal' wavenumber is indicated below.

Coney & Mobbs (1969–70) (comparable results were obtained for the smooth entry). In the same fashion as in § 3, we obtain results for e up to 0.6, Re_z up to 50 and Re_Ω up to 250, reaching reasonable accuracy with $N_\xi = K_\phi = 16$, as indicated in table 1.

4.1. *Critical azimuthal Reynolds number*

Compared to the wide-gap case, the critical Re_Ω are higher, which is as expected because the curvature of the gap is less important. The transition to higher-order LH modes happens at much lower advection rates, and $m = 5$ becomes critical before $Re_z = 50$ for some eccentricities. Unlike for $\eta = 0.5$, increasing the eccentricity at a fixed Re_z results in the selection of higher-order m. For the wide gap, this was the case only for TV and LH1 (for low e), and otherwise selection of lower-order m was observed. Figure 14(*a*) shows how the critical curves for the different m lie close to each other ($e = 0.2$ here), including the first RH modes. Complex behaviour is expected in the supercritical régime from the competition of the different helices. Note that no weak destabilizing effect of advection is noticed for any value of $Re_z \leqslant 50$ at any eccentricity. Indeed, this effect is expected to be pushed towards much higher values of Re_z, as in the concentric case. In this case, Ng & Turner (1982) found such an effect to occur at about $Re_z \sim 10^3$ for $\eta = 0.77$ (extremely weak effect), and did not observe it at all for $\eta = 0.95$ and $Re_z \leqslant 6000$.

4.2. *Critical axial wavenumber*

The range of critical axial wavenumbers (figure 15) is almost the same as in the wide-gap case. This means that the clearance is still controlling the size of the vortices. The most noticeable difference with $\eta = 0.5$ is the fact that for weak eccentricities ($e \leqslant 0.2$) and low-order modes, k increases continuously with Re_z. This was observed only for TV and LH1 in the previous case, but is now seen for more modes. This observation, together with the previous subsection, shows that the behaviour is globally the same as for $\eta = 0.5$, but variation in critical m is much faster as Re_z increases and more modes are involved. This behaviour is consistent with the results of Ng & Turner

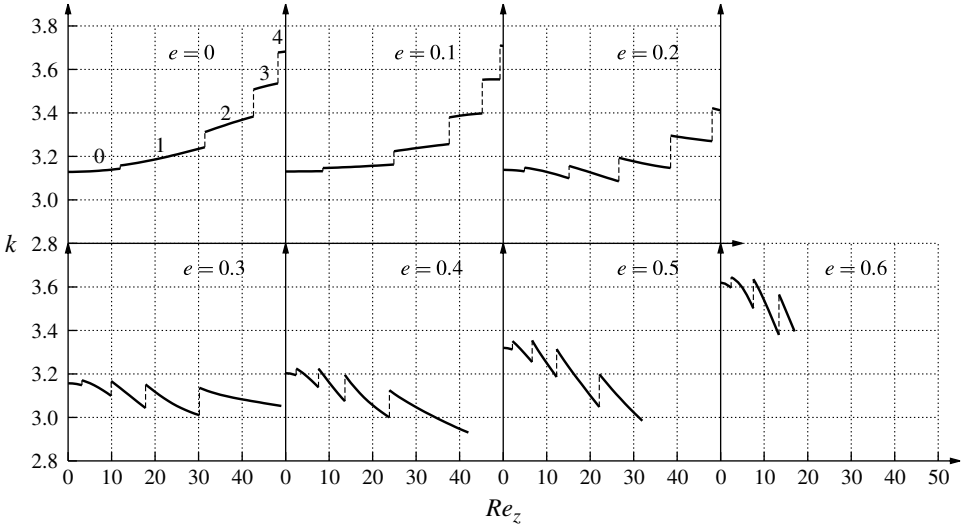

FIGURE 15. The critical wavenumber k against the axial Reynolds number Re_z for eccentricities $e = 0, 0.1, \ldots, 0.6$. Discontinuities correspond to a switch in critical m (values indicated by annotation for $e = 0$).

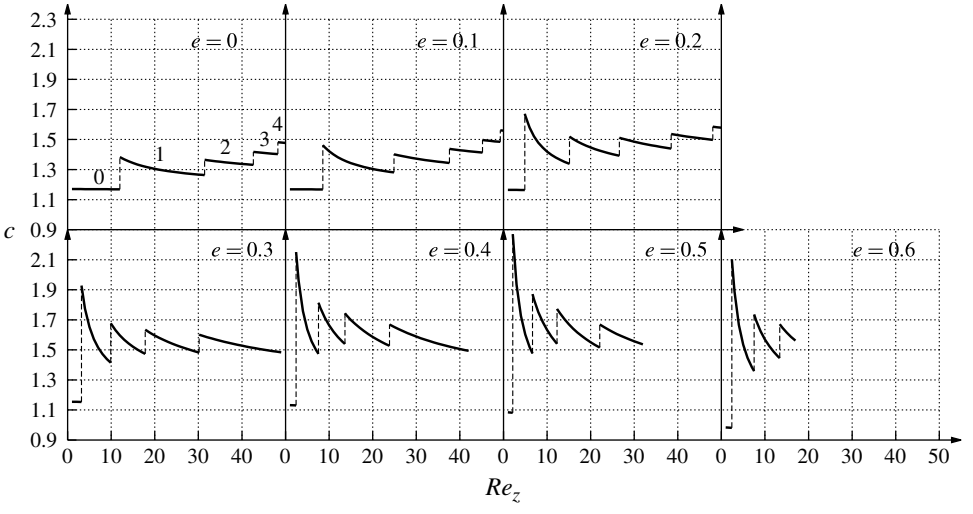

FIGURE 16. The critical phase speed c (in base flow axial speed unit $\overline{w_B}$) against the axial Reynolds number Re_z for eccentricities $e = 0, 0.1, \ldots, 0.6$. Discontinuities correspond to a switch in critical m (values indicated by annotation for $e = 0$).

(1982) who found a critical azimuthal wavenumber of 12 at $Re_z = 100$ for $\eta = 0.77$, and of 35 for $\eta = 0.95$.

4.3. *Critical phase speed*

As for the case $\eta = 0.5$, the phase speed is around 1–2 times the average axial speed of the base flow (figure 16). As the eccentricity is increased, the jump in phase speed

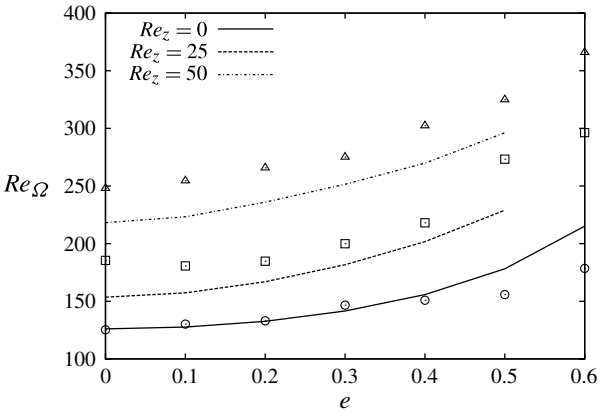

FIGURE 17. Comparison of the critical curves $Re_\Omega = f(e)$ for $Re_z = 0, 25, 50$: the present results (lines) and the experimental results (points) of Coney & Mobbs (1969–70) for the sharp entry apparatus.

between consecutive critical modes becomes larger. For high enough eccentricities, the peak phase speed is that of the LH1.

4.4. *Comparison with experiments*

In this section, we compare the numerical results with a series of experiments performed on a single apparatus of radius ratio $\eta = 0.89$ and aspect ratio (length over clearance) $L = 71.8$. Figure 17 compares experimental data from Coney & Mobbs (1969–70) (sharp entry case) against our calculations, after converting their graphical data into our system of control parameters. The agreement is quite good when there is no axial flow, and for $e < 0.5$. At higher eccentricities, though, we predict transition at higher rotation rates. It is likely that the difference is due to boundary effects, causing early transition to a Taylor 'pre-vortex' flow as reported in Mobbs & Ozogan (1984).

As soon as axial flow is added, the predicted critical Re_Ω is significantly lower than the experimental values, at any eccentricity, though the trends are the same. The experimental data lie between 10 and 20 % above the calculated threshold. Discrepancies as high as 20 % were also noticed between the numerical predictions of Ng & Turner (1982) and the experimental data of Nagib (1972) for the Taylor–Couette–Poiseuille flow of radius ratio $\eta = 0.77$. Takeuchi & Jankowski (1981) reported divergent trends between theoretical predictions and experimental data for $\eta = 0.5$ and Re_z as low as 40. Takeuchi & Jankowski (1981) claimed that the length of the apparatus was responsible for the supercritical Taylor numbers. Indeed, they invoked the idea of a 'vortex development length', defined as 'the length needed for a moving disturbance to reach an amplitude that is observable by the visualization method'. With more recent theory, it would be said that the instability is convective and is triggered by noise at the inlet of the apparatus (sharp or smooth). Indeed, the apparatus used by Coney & Mobbs (1969–70) is quite compact compared to other experiments. The length to gap ratio L is 71.8, whereas it was 160 for Nagib (1972) and 110 for Takeuchi & Jankowski (1981), respectively. In comparison, for a radius ratio of $\eta = 0.95$ and a length to gap ratio of 290, Snyder (1962) obtained experimental data that match those of Ng & Turner (1982) very closely, supporting the idea of the importance of the vortex development length. As advection is increased,

Re_z	Torque (1)	Visual (1)	Visual (1)	Visual (2)	Visual (3)	Present work
0	145	175	166	162	164	178
25	208	269	219	249	301	229
50	281	349	303	334	319	296

TABLE 2. Critical Re_Ω for $e = 0.5$, $\eta = 0.89$: (1), Younes (1972); (2), Coney & Mobbs (1969–70) and Coney (1971); (3), Coney & Atkinson (1978).

m	k	$\omega_{i,max}$	c	c_g	$-k_i$	$\exp[-k_i L]$
-1	2.60	1.95×10^{-4}	0.89	1.08	0.0010	1.1
0	2.70	9.04×10^{-3}	1.03	1.09	0.0455	26.3
1	2.82	1.55×10^{-2}	1.16	1.10	0.0774	258.3
2	2.94	2.00×10^{-2}	1.28	1.12	0.0986	1187.6
3	3.08	2.28×10^{-2}	1.39	1.13	0.1112	2943.3
4	3.21	2.43×10^{-2}	1.50	1.14	0.1169	4429.7
5	3.37	2.46×10^{-2}	1.60	1.16	0.1171	4488.0
6	3.53	2.40×10^{-2}	1.69	1.17	0.1131	3356.9

TABLE 3. Properties of the unstable modes $m = -1, \ldots, 6$ for $e = 0.3$, $Re_z = 50$ and $Re_\Omega = 275$. k and $\omega_{i,max}$ are calculated from the temporal stability problem. The phase speed c and the group velocity c_g are relative to the average axial flow velocity $\overline{w_B}$. k_i is the spatial amplification rate from Gaster (1962)'s relation. $\exp[-k_i L]$ is the amplification factor from the inlet to the outlet of the apparatus (Coney & Mobbs 1969–70).

perturbations travel faster as they grow, and might not be detected for large Re_z, which also explains why the results diverge for larger Re_z.

In table 2, numerical values are given for the critical Re_Ω at $e = 0.5$, from visual observations and torque measurements, compared to our values. The table shows significant scatter of the experimental data, even when using the same technique; for example, visual observations. Values obtained via torque measurements always give lower values than those from visualization, as the method is essentially more sensitive to the 'pre-vortex' flow located near the inner cylinder and difficult to visualize. Overall, the theoretical values always lie within (or very close to) the bounds given by the experiments.

4.5. *The 'double-vortex' pattern*

More surprising are the complex patterns observed by Coney & Mobbs (1969–70), with an apparently random axial wavenumber. For an eccentricity of $e = 0.3$ and an axial Reynolds number of $Re_z = 50$, they described a system of two vortices coexisting in the annulus: a left and a right helix, respectively. Looking at their graph, the azimuthal Reynolds number associated with this state has a supercritical value of $Re_\Omega \approx 275$. For this set of parameters, it is possible to calculate the maximum growth rate of all unstable modes. The results are reported in table 3, including the axial wavenumber, the phase speed and the group velocity $c_g \equiv \partial\omega_r/\partial k$. Modes $m = -1$ to 6 are all linearly unstable, so theory allows for a RH to grow at these operating conditions. However, the growth rates associated with higher-order LH are much higher, and $m = 5$ is dominant, closely followed by $m = 4$. The wavenumbers of these

latter modes lie in the lower range of what was experimentally observed: 3.25–5.20. Temporal stability theory offers no obvious explanation for the larger wavenumber perturbations observed in the experiment.

In table 3, we also give the equivalent spatial amplification properties of the unstable modes, following Gaster (1962). For near-critical perturbations, the spatial amplification rate $-k_i$ can be related to the temporal growth rate ω_i, via the group velocity of the perturbation, with the simple relation $-k_i \approx \omega_i/c_g$. In the spatial stability framework (meaningful for convective instabilities), the resulting amplification of the perturbations over the length L of the apparatus is given by $\exp[-k_i L]$. According to this theory, the spatial amplification of higher-order spirals is very fast due to the large growth rate and the moderate group velocity. On the other hand, RH spiral $m = -1$ is barely amplified through the apparatus and is very unlikely to saturate before exiting the system.

One could then think of this unexpected pattern as a consequence of transient growth due to non-modal effects (for a review, see Chomaz 2005). Heaton (2008) assessed the importance of these effects in axisymmetric Taylor–Couette–Poiseuille flow, and showed that they could also potentially explain deviations from modal stability predictions at moderate Re_z, typically of the order of a few hundreds. For lower Re_z, however, transient growth is not significant, and modal theory alone was shown (Cotrell *et al.* 2004) to match the experimental results accurately. Hence, for $Re_z = 50$, it seems unlikely that transient effects might be important, even though no results are currently available for the eccentric case.

Owing to the supercritical operating conditions and the variety of unstable modes, nonlinear simulations would surely help us to understand the double-vortex pattern. As in the case with no advection, end effects might also have an impact on the stability properties. Finally, phase noise may prevent a clear identification of the convectively amplified pattern (Babcock, Ahlers & Cannell 1991; Babcock, Cannell & Ahlers 1992).

5. Conclusions and perspectives

The temporal stability of eccentric Taylor–Couette–Poiseuille flow with a fixed outer cylinder has been investigated for a large range of parameter space. Parametric studies have been performed for a wide-gap case $\eta = 0.5$ with $Re_z \leqslant 200$ and $e \leqslant 0.7$, and a small-gap case $\eta = 0.89$ with $Re_z \leqslant 50$ and $e \leqslant 0.6$. Taylor vortices give way to helical structures of increasing azimuthal complexity as advection is increased. The helicity of these structures is always opposed to the inner-cylinder rotation, and are termed left helices, as in Taylor–Couette–Poiseuille flow. Broken axisymmetry changes the thresholds and distorts the critical modes, but was not found to trigger any new instability mechanism for the parameter range considered.

Eccentricity is always stabilizing, regardless of the axial flow rate, and this effect becomes even more important for higher values of e. Indeed, centrifugal effects are weakened at $e \geqslant 0.3$, as a low-speed recirculation region forms in the base flow and less fluid is driven in rotation around the inner cylinder. The effect of axial advection at fixed eccentricities is more subtle. For the small-gap case, the critical Re_Ω increases steadily with Re_z. For the wide-gap case $\eta = 0.5$, the critical Re_Ω increases for weak values of Re_z, but decreases slightly as axial advection is increased further. The maximum value of the critical Re_Ω is obtained for a value of Re_z that increases with eccentricity. Despite the destabilizing effect of advection above this specific value of Re_z, the case with no advection always remains the most unstable. For the wider

gap $\eta = 0.5$, increasing e at fixed Re_z tends to lower the critical pseudo-azimuthal wavenumber m (except for LH1 over TV), whereas 'higher-order' modes seem to be selected for $\eta = 0.89$. The critical axial wavelength is always of the order of the clearance d. For $\eta = 0.5$, the axial wavenumber k decreases continuously for a given m (except for TV and LH1 at small eccentricities) with increasing Re_z, but positive jumps are seen as higher and higher pseudo-azimuthal wavenumber m are selected at criticality. For $\eta = 0.89$, the behaviour is similar except that the increase of k for small m and small e is seen for more modes. For both radius ratios, the critical phase speed c of the travelling waves varies between 0.8 and 2.2 times the axial mean velocity of the base flow. c decreases with Re_z, except when the critical azimuthal wavenumber switches, in which case there is a discontinuous jump to a higher phase speed. For the small-gap case $\eta = 0.89$, the range of Re_z for which a critical fixed m dominates is much smaller than for $\eta = 0.5$ and transition to higher-order modes happens in a smoother way as Re_z increases. Mode competition is more pronounced for the small-gap case because modes of different m lie closer to each other in the (Re_Ω, Re_z) plane.

Whereas the instability mechanism for TV is only centrifugal, with a stabilizing effect of Re_z, the destabilization of helical modes $m > 0$ is strongly influenced by axial advection. Indeed, higher-order LH modes require a minimum amount of axial shear to become unstable, and this effect dominates the centrifugal mechanism for low Re_z. For large enough Re_z, the effect of axial advection becomes minor, compared to centrifugal destabilization with increasing Re_Ω. Maximum vortex activity, measured here by the maximum of the disturbance kinetic energy, is localized in the converging gap and moves towards the small gap and inner cylinder as Re_z is increased. At the same time, the disturbance energy concentrates increasingly into axial motion, recalling the two-dimensional structure of TS waves generated by axial shear. However, the so-called TS-like disturbances, involving a critical layer close to the wall, are not found in the range of the computations and are only expected to appear at larger advection rates (Cotrell & Pearlstein 2004). Centre modes of *Sp* type, found in eccentric annular Poiseuille flow by Merzari *et al.* (2008), are expected to exist in eccentric Taylor–Couette–Poiseuille flow at sufficiently large values of Re_z, but would require prohibitively fine meshing to be explored thoroughly with the method used here.

Comparison with the experiment of Coney & Mobbs (1969–70) for the small-gap case shows agreement within 20 % and matching trends. However, transition is found to occur below the linear threshold for $e \geqslant 0.5$ and $Re_z = 0$, and above for $Re_z = 25$ and 50 regardless of e. These differences are thought to be due to finite-length effects. In the eccentric case with no axial flow, end effects may be responsible for the onset of toroidal vortices below the limit of infinite-cylinder theory. When axial flow is added, delayed onset is probably caused by the 'vortex development length' invoked by Takeuchi & Jankowski (1981). In the framework of convective instabilities, the system needs to be of appropriate length for the perturbations to reach an amplitude detectable by experiments. The apparatus being quite compact, it is plausible that high rotation rates would be needed to amplify perturbations before they exit the system. Despite encouraging results overall, modal stability analysis cannot fully explain the complex pattern observed for $e = 0.3$, $Re_z = 50$, involving a double-vortex structure. Non-modal effects, potentially responsible for transient amplification of this unexpected structure, are likely to be weak for such a low advection rate. According to Heaton (2008), these effects become important for Re_z of the order of a few hundreds in the concentric case, and might contribute to discrepancies in onset

of instability. Assuming that non-modal effects are also important at high Re_z for the eccentric case, we leave the calculation of optimal perturbations as a perspective. The double-vortex structure may result from nonlinear interactions between modes, and fully nonlinear simulations, including end effects and inlet noise, would be very helpful in understanding the formation of this pattern. More experimental data would also be appreciated to ensure reproducibility of the observations.

Although the experiments of Coney & Mobbs (1969–70) suggest that instability is triggered by noise at the inlet and amplified convectively, the effect of eccentricity on absolute instabilities (Huerre & Monkewitz 1985, 1990) remains an open problem. This aspect is currently being investigated and will be addressed in a future paper. A weakly nonlinear study is also required to determine whether the bifurcation remains supercritical over the whole parameter space, or if subcritical transition can occur. Possible steps towards a better understanding of annular flows of drilling muds include non-Newtonian effects and motion of the inner cylinder, as complex effects are expected (Escudier *et al.* 2002; Feng & Fu 2007; Feng *et al.* 2007). To fully document the linear stability properties of this flow, it would also be interesting to investigate the connection with eccentric annular Poiseuille flow at high Re_z, analysed by Cotrell & Pearlstein (2004) and Cotrell *et al.* (2004) in the concentric case. At high Re_z, three families of modes of very different structure are expected to compete (Merzari *et al.* 2008) and make the problem even more computationally challenging.

Appendix

This appendix contains, in non-dimensional form, the expression of some differential operators using Wood (1957)'s modified bipolar coordinate system defined by (2.4)–(2.6). As in § 2.2, the 'stretched' variable defined by $\xi = (2\rho - \alpha - 2)/\alpha$ (where $\alpha = \beta - 1$) is used instead of ρ to transform the flow domain to $-1 \leqslant \xi \leqslant 1$. Following DiPrima & Stuart (1972*a*), the infinitesimal length element ds in (ξ, ϕ, z) is as follows:

$$\mathrm{d}s^2 = \frac{\alpha^2}{4\delta^2 J}\,\mathrm{d}\xi^2 + \frac{\rho^2}{\delta^2 J}\,\mathrm{d}\phi^2 + \mathrm{d}z^2, \tag{A 1}$$

where J the Jacobian of the transformation (2.4), given by

$$J = \frac{\left(1 + 2\gamma\rho\cos\phi + \gamma^2\rho^2\right)^2}{\left(1 - \gamma^2\right)^2}. \tag{A 2}$$

Introducing the inverse scale factors μ_ξ and μ_ϕ associated to the coordinates ξ and ϕ, respectively,

$$\mu_\xi = \frac{2\delta\sqrt{J}}{\alpha}, \quad \mu_\phi = \frac{\delta\sqrt{J}}{\rho}, \tag{A 3}$$

one can define the operators

$$D_\xi \equiv \mu_\xi \partial_\xi, \quad D_\phi \equiv \mu_\phi \partial_\phi, \tag{A 4}$$

and factors

$$A \equiv \mu_\phi - \partial_\xi \mu_\xi, \quad B \equiv \partial_\phi \mu_\phi, \quad C \equiv D_\xi A - D_\phi B. \tag{A 5}$$

Using Whitham (1963)'s general orthogonal coordinate formulas, the different terms in (2.2)–(2.3) can be written (recall that $\partial_z \equiv 0$ for the basic flow) as follows:

$$\boldsymbol{\nabla}_\perp p \equiv \begin{bmatrix} D_\xi p \\ D_\phi p \end{bmatrix}, \tag{A 6}$$

$$\boldsymbol{\nabla}_\perp \cdot \boldsymbol{u}_\perp \equiv (D_\xi + A)u + (D_\phi - B)v, \tag{A 7}$$

$$\boldsymbol{u}_\perp \cdot \boldsymbol{\nabla}_\perp \boldsymbol{u}_\perp \equiv \left(uD_\xi + vD_\phi\right)\boldsymbol{u} + (Av + Bu)\begin{bmatrix} -v \\ u \end{bmatrix}, \tag{A 8}$$

$$\boldsymbol{u}_\perp \cdot \boldsymbol{\nabla}_\perp w \equiv \left(uD_\xi + vD_\phi\right) w, \tag{A 9}$$

$$\nabla_\perp^2 \boldsymbol{u}_\perp \equiv \begin{bmatrix} \nabla_\perp^2 u \\ \nabla_\perp^2 v \end{bmatrix} + \begin{bmatrix} Cu - 2\left(AD_\phi + BD_\xi\right)v \\ Cv + 2\left(AD_\phi + BD_\xi\right)u \end{bmatrix}, \tag{A 10}$$

where the scalar Laplacian has the expression

$$\nabla_\perp^2 \equiv D_\xi^2 + D_\phi^2 + (AD_\xi - BD_\phi). \tag{A 11}$$

Finally, we give the expression for the rate-of-strain tensor in-plane components used for force/torque calculations:

$$\begin{cases} e_{\xi\xi} = D_\xi u - Bv, \\ e_{\phi\phi} = D_\phi v + Au, \\ e_{\phi\xi} = e_{\xi\phi} = \frac{1}{2}(D_\xi v + D_\phi u + Bu - Av). \end{cases} \tag{A 12}$$

REFERENCES

ALTMEYER, S., HOFFMANN, C. & LÜCKE, M. 2011 Islands of instability for growth of spiral vortices in the Taylor–Couette system with and without axial through flow. *Phys. Rev.* E **84**, 046308.

ARNOLDI, W. E. 1951 The principle of minimized iterations in the solution of the matrix eigenvalue problem. *Q. Appl. Maths* **9**, 17–29.

BABCOCK, K. L., AHLERS, G. & CANNELL, D. S. 1991 Noise-sustained structure in Taylor–Couette flow with through flow. *Phys. Rev. Lett.* **67**, 3388–3391.

BABCOCK, K. L., CANNELL, D. S. & AHLERS, G. 1992 Stability and noise in Taylor–Couette flow with through-flow. *Physica* D **61** (1), 40–46.

CASTLE, P. & MOBBS, F. R. 1967 Hydrodynamic stability of the flow between eccentric rotating cylinders: visual observations and torque measurements (paper 6). In *Institution of Mechanical Engineers, Conference Proceedings*, vol. 182, pp. 41–52.

CHANDRASEKHAR, S. 1960 The hydrodynamic stability of viscid flow between coaxial cylinders. *Proc. Natl Acad. Sci. USA* **46**, 141–143.

CHANDRASEKHAR, S. 1981 *Hydrodynamic and Hydromagnetic Stability*. Dover.

CHAWDA, A. & AVGOUSTI, M. 1996 Stability of viscoelastic flow between eccentric rotating cylinders. *J. Non-Newtonian Fluid Mech.* **63**, 97–120.

CHOMAZ, J.-M. 2005 Global instabilities in spatially developing flows: non-normality and nonlinearity. *Annu. Rev. Fluid Mech.* **37**, 357–392.

COLE, J. A. 1957 Experiments on the flow in rotating annular clearances (paper 15). In *Proceedings of the Conference on Lubrication and Wear*, pp. 16–19. Institution of Mechanical Engineers.

COLE, J. A. 1967 Taylor vortices with eccentric rotating cylinders. *Nature* **216**, 1200–1202.

COLE, J. A. 1969 Taylor vortices with eccentric rotating cylinders. *Nature* **221**, 253–254.

CONEY, J. E. R. 1971 Taylor vortex flow with special reference to rotary heat exchangers. PhD thesis, University of Leeds.

CONEY, J. E. R. & ATKINSON, J. 1978 The effect of Taylor vortex flow on the radial forces in an annulus having variable eccentricity and axial flow. *Trans. ASME: J. Fluids Engng* **100**, 210–214.

CONEY, J. E. R & MOBBS, F. R. 1969–70 Hydrodynamic stability of the flow between eccentric rotating cylinders with axial flow: visual observations (paper 2). *Proc. Inst. Mech. Engrs* **184 Pt 3L**, 10–17.

COTRELL, D. L. & PEARLSTEIN, A. J. 2004 The connection between centrifugal instability and Tollmien–Schlichting-like instability for spiral Poiseuille flow. *J. Fluid Mech.* **509**, 331–351.

COTRELL, D. L., SARMA, L. R. & PEARLSTEIN, A. J. 2004 Computational assessment of subcritical and delayed onset in spiral Poiseuille flow experiments. *J. Fluid Mech.* **509**, 353–378.

DAI, R.-X., DONG, Q. & SZERI, A. Z. 1992 Flow between eccentric rotating cylinders: bifurcation and stability. *Intl J. Engng Sci.* **30**, 1323–1340.

DIPRIMA, R. C. 1959 The stability of viscous flow between rotating concentric cylinders with a pressure gradient acting round the cylinders. *J. Fluid Mech.* **6**, 462–468.

DIPRIMA, R. C. 1960 The stability of a viscous fluid between rotating cylinders with an axial flow. *J. Fluid Mech.* **9**, 621–631.

DIPRIMA, R. C. 1963 A note on the stability of flow in loaded journal bearings. *Trans. Am. Soc. Lubric. Engrs* **6**, 249–253.

DIPRIMA, R. C., EAGLES, P. M. & NG, B. S. 1984 The effect of radius ratio on the stability of Couette flow and Taylor vortex flow. *Phys. Fluids* **27**, 2403–2411.

DIPRIMA, R. C. & STUART, J. T. 1972*a* Flow between eccentric rotating cylinders. *J. Lubric. Tech.* **94**, 266–274.

DIPRIMA, R. C. & STUART, J. T. 1972*b* Non-local effects in the stability of flow between eccentric rotating cylinders. *J. Fluid Mech.* **54**, 393–415.

DIPRIMA, R. C. & STUART, J. T. 1975 The nonlinear calculation of Taylor vortex flow between eccentric rotating cylinders. *J. Fluid Mech.* **67**, 85–111.

DRIS, I. M. & SHAQFEH, E. S. G. 1998 Experimental and theoretical observations of elastic instabilities in eccentric cylinder flows: local versus global instability. *J. Non-Newtonian Fluid Mech.* **80**, 1–58.

EAGLES, P. M., STUART, J. T. & DIPRIMA, R. C. 1978 The effects of eccentricity on torque and load in Taylor-vortex flow. *J. Fluid Mech.* **87**, 209–231.

EL-DUJAILY, M. J. & MOBBS, F. R. 1990 The effect of end walls on subcritical flow between concentric and eccentric rotating cylinders. *Intl J. Heat Fluid Flow* **11**, 72–78.

ESCUDIER, M. P., GOULDSON, I. W., OLIVEIRA, P. J. & PINHO, F. T. 2000 Effects of inner cylinder rotation on laminar flow of a Newtonian fluid through an eccentric annulus. *Intl J. Heat Fluid Flow* **21**, 92–103.

ESCUDIER, M. P., OLIVEIRA, P. J. & PINHO, F. T. 2002 Fully developed laminar flow of purely viscous non-Newtonian liquids through annuli, including the effects of eccentricity and inner-cylinder rotation. *Intl J. Heat Fluid Flow* **23**, 52–73.

FENG, S. & FU, S. 2007 Influence of orbital motion of inner cylinder on eccentric Taylor vortex flow of Newtonian and power-law fluids. *Chin. Phys. Lett.* **24**, 759–762.

FENG, S., LI, Q. & FU, S. 2007 On the orbital motion of a rotating inner cylinder in annular flow. *Intl J. Numer. Meth. Fluids* **54**, 155–173.

FRÊNE, J. & GODET, M. 1971 Transition from laminar to Taylor vortex flow in journal bearings. *Tribology* **4**, 216–217.

GASTER, M. 1962 A note on the relation between temporally-increasing and spatially-increasing disturbances in hydrodynamic stability. *J. Fluid Mech.* **14**, 222–224.

GODA, K. 1979 A multistep technique with implicit difference schemes for calculating two- or three-dimensional cavity flows. *J. Comput. Phys.* **30**, 76–95.

GUO, B. & LIU, G. 2011 *Applied Drilling Circulation Systems – Hydraulics, Calculations, Models*. Elsevier.

HEATON, C. J. 2008 Optimal linear growth in spiral Poiseuille flow. *J. Fluid Mech.* **607**, 141–166.

HUERRE, P. & MONKEWITZ, P. A. 1985 Absolute and convective instabilities in free shear layers. *J. Fluid Mech.* **159**, 151–68.

HUERRE, P. & MONKEWITZ, P. A. 1990 Local and global instabilities in spatially developing flows. *Annu. Rev. Fluid. Mech.* **22**, 473–537.

HUGGINS, N. J. 1966–67 Tests on a 24-in diameter journal bearing: transition from laminar to turbulent flow. In *Symposium on Journal Bearings for Reciprocating and Turbo Machinery, Proc. Inst. Mech. Engrs*, vol. 181 (Pt 3B), p. 81.

HWANG, J. Y. & YANG, K. S. 2004 Numerical study of Taylor–Couette flow with an axial flow. *Comput. Fluids* **33**, 97–118.

KAMAL, M. M. 1966 Separation in the flow between eccentric rotating cylinders. *Trans. ASME J. Basic Engng* **88**, 717–724.

KARASUDANI, T. 1987 Non-axis-symmetric Taylor vortex flow in eccentric rotating cylinders. *J. Phys. Soc. Japan* **56**, 855–858.

KOSCHMIEDER, E. L. 1976 Taylor vortices between eccentric cylinders. *Phys. Fluids* **19**, 1–4.

LIM, T. T. & LIM, S. S. 2008 Modified expression for critical Reynolds number in eccentric Taylor–Couette flow. *AIAA J.* **46**, 277–280.

MACKRODT, P. A. 1976 Stability of Hagen–Poiseuille flow with superimposed rigid rotation. *J. Fluid Mech.* **73**, 153–164.

MARQUES, F. & LOPEZ, J. M. 2000 Spatial and temporal resonances in a periodically forced hydrodynamic system. *Physica* D **136**, 340–352.

MARTINAND, D., SERRE, E. & LUEPTOW, R. M. 2009 Absolute and convective instability of cylindrical Couette flow with axial and radial flows. *Phys. Fluids* **21**, 104102.

MERZARI, E., WANG, S., NINOKATA, H. & THEOFILIS, V. 2008 Biglobal linear stability analysis for the flow in eccentric annular channels and a related geometry. *Phys. Fluids* **20**, 114104.

MESEGUER, A. & MARQUES, F. 2000 On the competition between centrifugal and shear instability in spiral Couette flow. *J. Fluid Mech.* **402**, 33–56.

MESEGUER, A. & MARQUES, F. 2002 On the competition between centrifugal and shear instability in spiral Poiseuille flow. *J. Fluid Mech.* **455**, 129–148.

MOBBS, F. R. & OZOGAN, M. S. 1984 Study of sub-critical Taylor vortex flow between eccentric rotating cylinders by torque measurements and visual observations. *Intl J. Heat Fluid Flow* **5**, 251–253.

MOBBS, F. R. & YOUNES, M. A. M. A. 1974 The Taylor vortex regime in the flow between eccentric rotating cylinders. *Trans. ASME: J. Lubric. Tech.* 127–134.

NAGIB, H. 1972 On instabilities and secondary motions in swirling flows through annuli. PhD thesis, Illinois Institute of Technology.

NG, B. S. & TURNER, E. R. 1982 On the linear stability of spiral flow between rotating cylinders. *Proc. R. Soc. Lond.* A *Mat.* **382**, 83–102.

OIKAWA, M., KARASUDANI, T. & FUNAKOSHI, M. 1989*a* Stability of flow between eccentric rotating cylinders. *J. Phys. Soc. Japan* **58**, 2355–2364.

OIKAWA, M., KARASUDANI, T. & FUNAKOSHI, M. 1989*b* Stability of flow between eccentric rotating cylinders with a wide gap. *J. Phys. Soc. Japan* **58**, 2209–2210.

PODRYABINKIN, E. V. & RUDYAK, V. Y. 2011 Moment and forces exerted on the inner cylinder in eccentric annular flow. *J. Engng Thermophys.* **20**, 320–328.

RASPO, I., HUGUES, S., SERRE, E., RANDRIAMAMPIANINA, A. & BONTOUX, P. 2002 A spectral projection method for the simulation of complex three-dimensional rotating flows. *Comput. Fluids* **31**, 745–767.

REID, W. H. 1961 Review of The hydrodynamic stability of viscid flow between coaxial cylinders by S. Chandrasekhar (*Proc. Natl Acad. Sci. USA***46**, 141–143, 1960). *Math. Rev.* **22**, 565.

RITCHIE, G. S. 1968 On the stability of viscous flow between eccentric rotating cylinders. *J. Fluid Mech.* **32**, 131–144.

SEP, J. 2008 Journal bearing with an intensive axial oil flow–experimental investigation. *Scientific Problems of Machines Operation and Maintenance* **43**, 21–29.

SNYDER, H. A. 1962 Experiments on the stability of spiral flow at low axial Reynolds numbers. *Proc. R. Soc. Lond.* A *Mat.* **265**, 198–214.

SNYDER, H. A. 1965 Experiments on the stability of two types of spiral flow. *Ann. Phys.* **31**, 292–313.

TAKEUCHI, D. I. & JANKOWSKI, D. F. 1981 Numerical and experimental investigation of the stability of spiral Poiseuille flow. *J. Fluid Mech.* **102**, 101–26.

TAYLOR, G. I. 1923 Stability of a viscous liquid contained between two rotating cylinders. *Phil. Trans. R. Soc. Lond.* **223**, 289–343.

VERSTEEGEN, P. L. & JANKOWSKI, D. F. 1969 Experiments on the stability of viscous flow between eccentric rotating cylinders. *Phys. Fluids* **12**, 1138–1143.

VOHR, J. A. 1968 An experimental study of Taylor vortices and turbulence in flow between eccentric rotating cylinders. *Trans. ASME: J. Lubric. Tech.* **90**, 285–296.

WANNIER, G. H. 1950 A contribution to the hydrodynamics of lubrication. *Q. Appl. Maths* **8**, 1–32.

WHITHAM, G. B. 1963 The Navier–Stokes equations of motion. In *Laminar boundary layers* (ed. L. Rosenhead), chap. III, Clarendon.

WOOD, W. W. 1957 The asymptotic expansions at large Reynolds numbers for steady motion between noncoaxial rotating cylinders. *J. Fluid Mech.* **3**, 159–175.

XIAO, Q., LIM, T. T. & CHEW, Y. T. 1997 Experimental investigation on the effect of eccentricity on Taylor–Couette flow. In *Transport Phenomena in Thermal Science and Process Engineering*, pp. 685–689. Kyoto, Japan.

YOUNES, M. A. M. A. 1972 The hydrodynamic stability of spiral flow between eccentric rotating cylinders. PhD thesis, University of Leeds.

YOUNES, M. A. M. A., MOBBS, F. R. & CONEY, J. E. R. 1972 Hydrodynamic stability of the flow between eccentric rotating cylinders with axial flow: torque measurements (paper C76/72). In *Tribology Convention, Institution of Mechanical Engineers*, pp. 14–19.